Journal of Hydrology 575 (2019) 1155–1177

Contents lists available at ScienceDirect

Journal of Hydrology

journal homepage: www.elsevier.com/locate/jhydrol

Research papers

Flood inundation modeling and mapping by integrating surface and subsurface hydrology with river hydrodynamics

Siddharth Saksena[a,*], Venkatesh Merwade[a], Peter J. Singhofen[b]

[a] Lyles School of Civil Engineering, 550 Stadium Mall Drive, Purdue University, West Lafayette, IN 47907, United States
[b] Streamline Technologies, Inc., 1900 Town Plaza Court, Winter Springs, FL 32708, United States

ARTICLE INFO

This manuscript was handled by Emmanouil Anagnostou, Editor-in-Chief

ABSTRACT

Modeling and mapping of floods using one (1D) and two-dimensional (2D) models has resulted in significant progress in our understanding of river hydraulics and hydrology. The existing modeling approach can be improved further through a better understanding of the interactions between river hydrodynamics and subsurface processes. Saturated conditions in subsurface and floodplains can lead to longer and deeper inundation from low intensity but continuous flood events. To understand the combined effect of surface-subsurface hydrology and hydrodynamics on streamflow generation and subsequent inundation during floods, this study uses an integrated surface water-groundwater (SW-GW) modeling approach for simulating flood conditions. Simulation of a high flooding event for the Upper Wabash River basin in Indiana, USA, shows that the river-floodplain hydrodynamics is simulated more accurately without the need for extensive calibration by using a two-dimensional integrated SW-GW model. Additionally, an integrated model provides a more realistic simulation of flood hydrodynamics for different antecedent soil conditions. Specifically, results show that the streamflow, flood stages and inundation area obtained for the dry scenario are significantly lower when compared to the saturated scenario. These findings are further validated by applying the integrated modeling approach for an entirely different watershed (Croton River) in the state of New York. Overall, the findings from this study suggest that the current practice of simulating floods which assumes an impervious surface may not be providing realistic estimates of flood inundation, and that an integrated approach incorporating all the hydrologic and hydraulic processes in the river system must be adopted.

1. Introduction

Most flood models are primarily driven by an upstream flow boundary condition to simulate the river hydrodynamics in one- or two dimensions to get the water surface elevation (WSE), velocity and extent of inundation for a study reach. The key inputs for this approach include topography to define the river geometry, streamflow, and the roughness coefficient (Manning's n). It is well documented in the literature that the current flood modeling approach is affected by several uncertainties arising from discharge estimates, topographic data, model selection, and parameterization, among others (Cook and Merwade, 2009; Hall et al., 2005; Legleiter et al., 2011; Merz and Thieken, 2005; Pappenberger et al., 2006; Saksena and Merwade, 2015; Straatsma and Huthoff, 2011). Some of these uncertainties can be addressed by using accurate topographic data at fine resolution (Bhuyian et al., 2015; Saksena and Merwade, 2015), accurate discharge data, and better model parameterization and calibration through satellite-based products (Cohen et al., 2018; Dey et al., 2019; Di Baldassarre et al., 2009; Schumann et al., 2007).

One of the limitations of simulating floods in rivers using a hydrodynamic model is that it cannot incorporate the interaction between the river reach and the subsurface, which can play a critical role in dictating the duration and extent of inundation. This interaction becomes even more critical when floods are simulated over a larger stream network as opposed to individual reaches. For example, models such as RAPID (Routing Application for Parallel Computation of Discharge), LISFLOOD-FP, and AutoRoute (Bates and De Roo, 2000; David et al., 2011b; Follum et al., 2016) have been applied at the river network scale, but these models simulate only the surface water hydrodynamics. One way these models compensate for excluding some of the related physical processes in the flood hydrodynamics is through the calibration of surface roughness in the form of the Manning's n parameter (Mukolwe et al., 2014; Pappenberger et al., 2005). This calibration is generally performed by estimating stage or streamflow at the

* Corresponding author.
E-mail address: ssaksena@purdue.edu (S. Saksena).

https://doi.org/10.1016/j.jhydrol.2019.06.024
Received 16 December 2018; Received in revised form 5 June 2019; Accepted 9 June 2019
Available online 11 June 2019

downstream model boundary. In some studies, the extent of inundation located inside the model domain (obtained from remote sensing) is used to calibrate roughness parameters (Di Baldassarre et al., 2009). Thus, the current hydrodynamic modeling approach assumes that the observed streamflow, stage and extent of inundation are solely functions of the roughness parameter distribution, upstream streamflow forcing and topography (Bales and Wagner, 2009; Dimitriadis et al., 2016; Teng et al., 2017). However, studies have shown that several combinations of roughness parameters, even unrealistic ones, can produce reasonable results for a specific event, but not necessarily for events outside the calibration range, especially for events with different antecedent conditions (Pappenberger et al., 2006, 2005). Nevertheless, this practice of ignoring physical processes variability has continued despite several studies concluding that the lack of linkage between surface water (SW) and groundwater (GW) contributions leads to uncertainties in the existing flood risk models (Kidmose et al., 2015; Pahar and Dhar, 2014; Panday and Huyakorn, 2004).

Numerous models exist to individually simulate overland flow, river hydraulics, and GW flow, but these models do not account for relative interactions between these processes (Fleckenstein et al., 2010; Faulkner et al., 2012; Osei-Twumasi et al., 2016). Additionally, several past studies have highlighted the importance of subsurface contributions and antecedent conditions on the streamflow hydrograph (Berthet et al., 2009; Cooper and Rorabaugh, 1963; Hughes et al., 2011; Moench et al., 1974), but how the SW-GW interaction affects the flow hydrodynamics between the river and its floodplain needs more investigation. This study is advocating that floods should be simulated using an integrated SW-GW modeling approach that is based on the solution of the mass balance equation at every time-step and can provide a more physical representation of the river-floodplain hydrodynamics by simultaneously incorporating physical processes such as precipitation, vadose zone storage, hydraulic routing, and GW flow. In the past, integrated SW-GW modeling procedures were deemed unsuitable primarily due to the absence of accurate data, and insufficient computational power (Grimaldi et al., 2013; Saleh et al., 2011). As a result, studies focused on creating tools for loosely coupling hydraulic and hydrologic models (David et al., 2011a; Jackson and Maidment, 2014), but these techniques fail to incorporate real-time impacts of SW-GW interaction in floodplains during high flows. With the increasing access to open source datasets and computational capabilities, more studies are focusing on using integrated SW-GW modeling procedures to simulate the hydrology and hydrodynamics of rivers (Gleeson and Manning, 2008; Kaser et al., 2014; Kollet and Maxwell, 2008; Liu et al., 2015; Saksena and Merwade, 2017a). However, many of these studies have focused on simulating hydrologic fluxes, such as streamflow, soil moisture and water table (WT) depth, without looking at how the interactions between some of these fluxes will affect the flood hydrodynamics and the subsequent inundation during a high flow event.

This study aims to address this gap by applying an integrated SW-GW model over a relatively large (area greater than 5000 km^2) watershed. Considering that an integrated SW-GW model provides a better streamflow prediction, this study hypothesizes that such a model will also provide more accurate and robust simulation of the flood hydrodynamics with less dependence on hydraulic model calibration using Manning's n. Specifically, this study aims to prove that both the upstream and downstream boundary conditions in a flood model are dynamic, and they are not only influenced by the surface water flow, but also by SW-GW interactions.

2. Study area and data

The Upper Wabash River (UWR) basin in Indiana (5840 km^2) is chosen as the test site for this study. The UWR basin is characterized by glacial till deposits, gentle slopes, fertile soils and shallow aquifers, with a deep confining layer of shale (Frisbee et al., 2017; Saksena and Merwade, 2017b). According to the National Resources Conservation Services' (NRCS) hydrologic soil group classification (Table 1), there is a dominance of soil group 'C' for the UWR basin, with an average vadose zone depth of 150 cm, and a shallow WT around the Wabash River. Although the watershed is primarily agricultural, the Wabash River floodplain consists of three major cities in Indiana, namely, Lafayette, Logansport, and Huntington. Additionally, according to the Flood Insurance Rate Maps (FIRMs) in this region, over 8% of the entire study area (468 km^2) falls under the 100-year 'flood zone'. Because of the existence of dams and control structures on the Wabash River, only the unregulated region in the UWR basin (shown in Fig. 1) is selected for this analysis. Table 1 presents a summary of the watershed characteristics for the study area. Considering the critical role of topography in hydrodynamic simulation of rivers (Saksena, 2015), a 9 m resolution topographic Digital Elevation Model (DEM) of high accuracy based on a LiDAR survey, obtained from the Indiana Spatial Data Portal (ISDP), is used in this study.

Table 1
Watershed characteristics.

Drainage Area, km^2	5840
Landuse as per NLCD 2011 (%)	
Agricultural	82
Forest	7
Water	2
Urban/Impervious	9
No. of NCDC rainfall weather stations	9
No. of USGS streamflow gages	9
Soil Type as per NRCS gSSURGO (%)	
A	2
B	36
C	61
D	1

The SW-GW integration for UWR basin is achieved by linking the unsaturated (vadose) zone with the overland flow region and the saturated zone (surficial aquifer). This type of modeling for a large area is data intensive and requires surface information in the form of topography, land use, and surface roughness (Manning's n); climate information in the form of rainfall and streamflow; and subsurface information in the form of vadose zone and aquifer properties. The land use data for the study are obtained from the National Land Cover Database (NLCD: http://nationalmap.gov/viewer.html). The values of Mannings' roughness corresponding to the eleven land use classes in NLCD are adapted from Chow (1959). Impervious cover data in the form of a raster grid is downloaded from the Indiana Map Data Server (USGS, 2006). For the subsurface part, vadose zone properties such as moisture content, vertical conductivity and soil type are characterized using information from the NRCSs' Gridded Soil Survey Geographic (gSSURGO) Database. Hourly rainfall data for the 9 climate stations in the UWR basin are obtained from the National Oceanic and Atmospheric Administration's (NOAA) Climate Data Online (CDO), and instantaneous streamflow and gage height data for 9 stations are obtained from the United States Geological Surveys' (USGS) National Water Information System (http://waterdata.usgs.gov/nwis/rt). Information on crop-type and frequency of crop plantation for calculating evapotranspiration rates is obtained from the 2011 National Cropland Data Layer (NCDL), which is developed by the United States Department of Agriculture (USDA: https://nassgeodata.gmu.edu/CropScape/).

Water surface elevations obtained from USGS gage data are used as an upstream boundary forcing for the Wabash River and its tributaries within the watershed. The outlet of the model is located at the USGS gage 03335500, Wabash River at Lafayette. Water table information in the form of contour maps are obtained from the Indiana Department of Natural Resources' (IDNR) Potentiometric Surface Maps (http://www.in.gov/dnr/water/7256.htm), which are converted into gridded raster formats at a spatial resolution of 30 m. using ArcGIS. Similarly, the shallow aquifer thickness information found in the Indiana Geographic Information Council's (IGIC) Indiana Map server (http://maps.indiana.

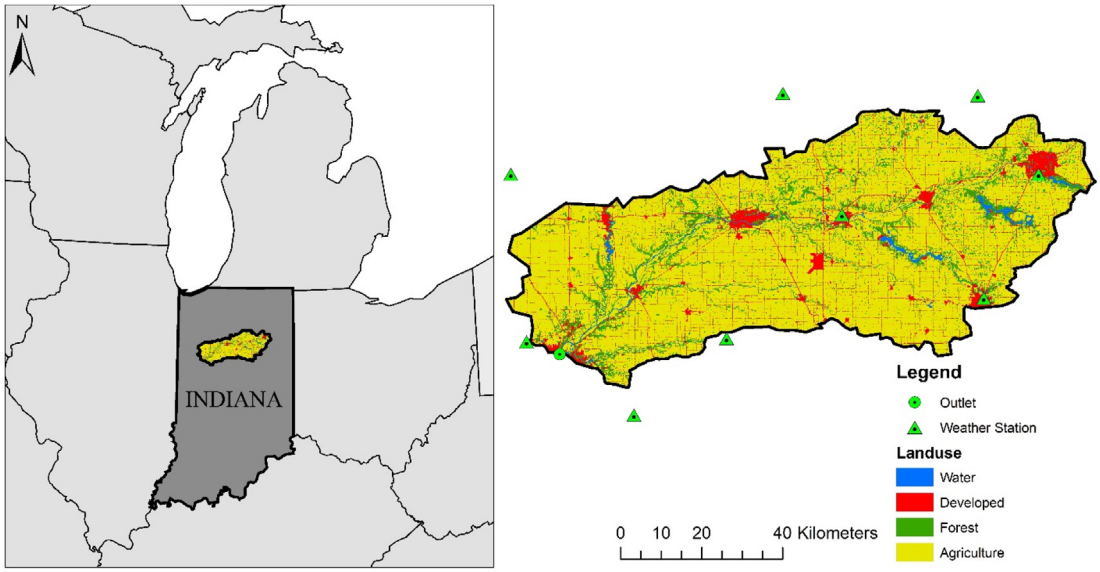

Fig. 1. Location and land use map for the unregulated portion of the UWR basin.

edu/index.html) is used for characterizing the surficial aquifer for the study area.

3. Model description

Several fully integrated models are available for simulating hydrologic responses from reach to continental scale using a distributed modeling approach (Paniconi and Putti, 2015), including but not limited to, the Integrated Hydrology Model (InHM: (VanderKwaak and Loague, 2001), GSSHA (Gridded Surface Subsurface Hydrologic Analysis: Downer et al., 2002; Downer and Ogden, 2006), ICPR (Streamline Technologies, 2018), DrainFlow (Shokri and Bardsley, 2016), ParFlow (Kollet and Maxwell, 2006; Maxwell et al., 2014), CATHY (Bixio et al., 2002), MIKE SHE (Hughes and Liu, 2008), tRIBS (Ivanov et al., 2004), HydroGeoSphere (Brunner and Simmons, 2012), and ADHydro (Ogden et al., 2014). However, considering the focus on flood inundation modeling and application over a large area, Interconnected Channel and Pond Routing (ICPR; Fig. 2) is used in this study. ICPR is a FEMA-approved integrated hydraulic and hydrologic model for the State of Florida that has been extensively validated for both SW and GW simulations across several watersheds in the United States (Streamline Technologies, 2016). ICPR is a two-dimensional (2D), integrated SW-GW modeling software, based on distributed model parameterization procedures (Streamline Technologies, 2018). The ICPR model has capabilities of combining precipitation, 2D surface flow, pond storage and GW simulations, for both event-based and continuous storm events (Ahmad et al., 2014; Booker, 2006; Jackson and Maidment, 2014; Joyce et al., 2017; Singhofen and McClung, 2014). As shown in Fig. 2, there are three basic components of an integrated ICPR model: (1) the surface system; (2) the vadose zone; and (3) the saturated groundwater system. Detailed description on these components including the methodology used to couple surface and subsurface systems is provided below.

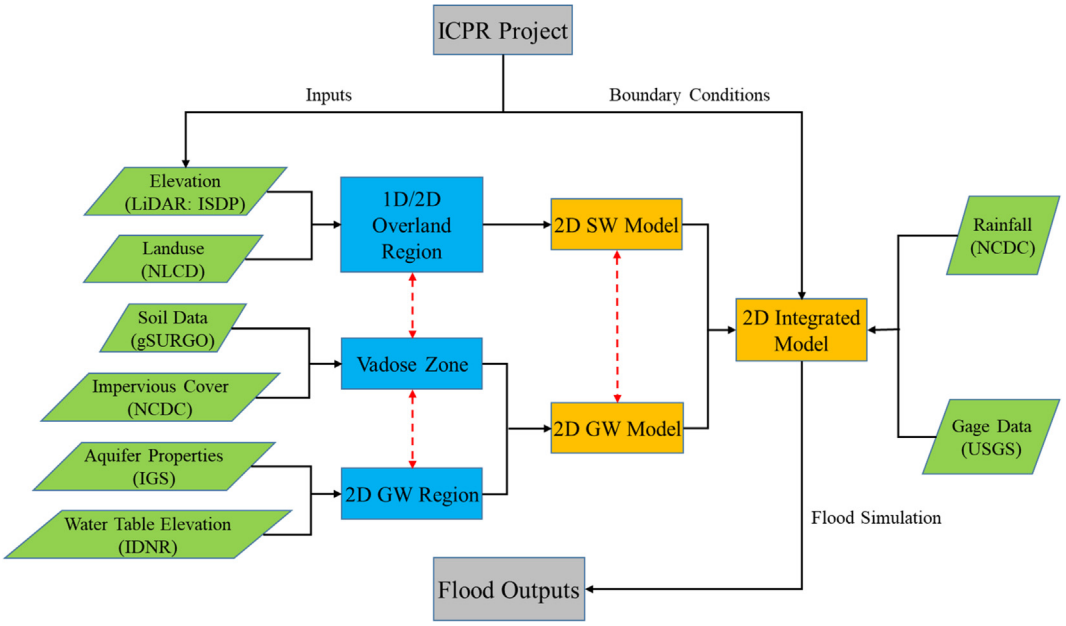

Fig. 2. ICPR project process diagram.

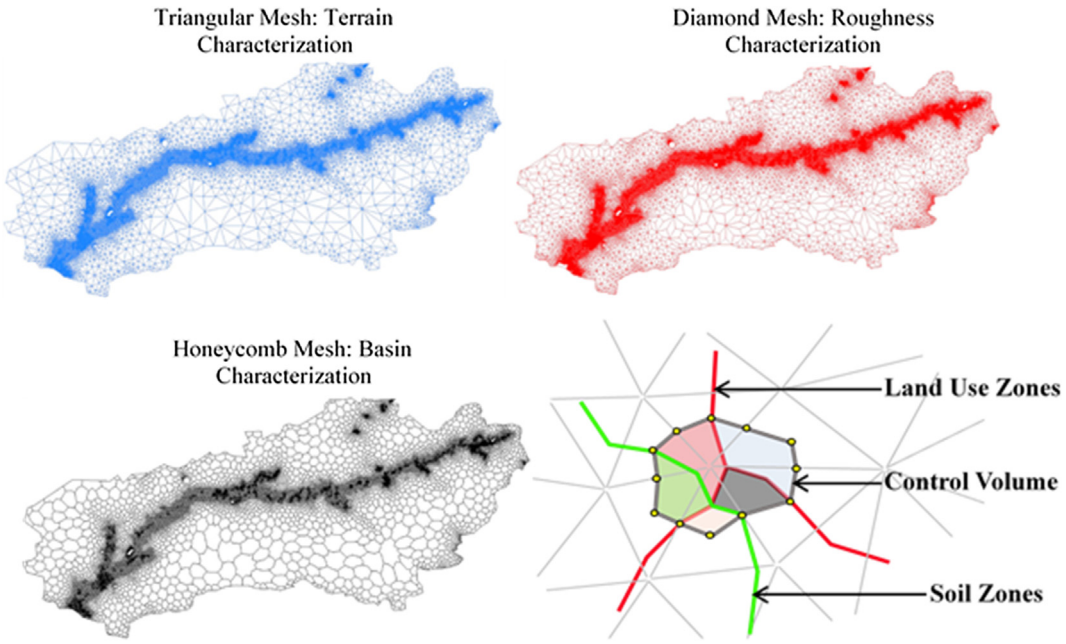

Fig. 3. Mesh structure within ICPR for the Upper Wabash Basin.

3.1. The surface system

ICPR uses a finite volume approach for surface flow using unstructured mesh networks. Momentum equations (with options for energy and diffusive wave equations) are lumped along triangle edges, and the mass balance equations (Appendix A, Eqs. (A.4)–(A.7)) are lumped at the triangle vertices where irregular shaped polygons are formed establishing local control volumes. This set of polygons is referred to as the surface honeycomb mesh. As shown in Fig. 3, the polygons are formed by connecting adjacent triangle midpoints and centroids. A diamond mesh is also formed along triangle edges for roughness classification (as shown in Fig. 3) and extends from vertices to adjacent triangle centroids (Streamline Technologies, 2018). The advantage of using unstructured networks in characterizing the topography and hydrologic processes is well documented in previous studies (Begnudelli and Sanders, 2006; Bunya et al., 2010).

ICPR allows the application of variable surface roughness for shallow and deep overland flow. During large flood events, the roughness changes over time when the depth of the water in the floodplain increases due to persistent flooding (Arcement and Schneider, 1984). Popular hydraulic models such as the Hydrologic Engineering Center's River Analysis System (HEC-RAS) and LISFLOOD-FP, do not account for this variability (Bates and De Roo, 2000; Brunner, 2010). ICPR uses an exponential decay function (presented in Appendix A, Eqs. (A.11) and (A.12)) dependent on surface depth to incorporate the variability in surface roughness. The shallow and deep roughness values corresponding to the NLCD land use classes are directly obtained from the maximum and minimum roughness values from Chow (1959) and are shown in Table 2.

3.2. The vadose zone

The vadose zone forms the primary communication link between the surface and groundwater systems. ICPR has several options for modeling the vadose zone (Streamline Technologies, 2018), including the Green-Ampt method (single homogeneous layer discretized into two cells), a refined Green-Ampt method (single homogeneous layer discretized into user specified number of computational cells), and the Vertical Layer method (soil properties vary by layer and each layer is further discretized into multiple cells). In all three cases, the Brooks-Corey soil water retention–hydraulic conductivity relationship (Rawls et al., 1982; Rawls and Brakensiek, 1982) is used to determine unsaturated conductivities based on current soil moisture contents. The refined Green-Ampt method is used in this study because it provides a more realistic distribution of soil moisture in the soil column compared to the standard Green-Ampt method. In this method, the soil moisture accounting and subsequent GW recharge from the vadose zone is computed using a non-iterative kinematic approach. Unlike the standard Green-Ampt method that permits only one soil moisture value within a single computational element (e.g. honeycomb or grid), the refined Green-Ampt allows the entire unsaturated soil zone to be divided into multiple cells (as illustrated in Fig. 4) which can contain different moisture contents based on the volume of water percolating into the vadose zone. In essence, the refined Green-Ampt method is identical to the Vertical Layer method except that the soil parameters are homogeneous for a given soil zone.

The non-iterative kinematic approach involves two passes through the various cells for every time-step. The first pass is from the ground surface downward to the last cell. Water enters the soil column at the top of the first cell based on an infiltration rate that cannot exceed the saturated vertical conductivity. The fluxes are calculated at the bottom of each cell based on the current moisture content in a cell and the corresponding unsaturated vertical conductivity as estimated by the Brooks-Corey method (Appendix A, Eq. (A.13)). A mass balance is performed for each cell based on the flux into the cell from its upper face minus the flux out of the cell across its bottom face. The moisture contents are updated based on the fluxes. The flux across the bottom face of the last cell is removed from the vadose zone and delivered to appropriate groundwater node. In the second pass, the cells are rebalanced from the bottom to the surface, to ensure that the moisture content in any cell does not exceed saturation. At this step, if any cell contains water in excess of saturation, the difference (excess water content) is moved upward to adjacent cells and eventually delivered to the surface system, if necessary. Since the WT is dynamic, the cells are "swallowed" as the WT moves upward. Therefore, if a cell is inundated by more than 75% due to the rising WT, it is merged with the saturated cell below it, and the soil moisture is redistributed accordingly. Similarly, as the WT drops, the moisture content of the newly exposed portion of a given cell is automatically set to field capacity. If more than 25% of a given cell is exposed, it becomes active again. The 75%

Table 2
ICPR uncalibrated subsurface and surface roughness parameters*.

No.	Vadose Zone	Description	A	B	C	D
1	K_v	Saturated vertical conductivity, mm/h	15.2	6.2	2.3	1.4
2	MCS	Moisture content at saturation	0.30	0.540	0.458	0.62
3	MCR	Residual moisture content	0.031	0.068	0.078	0.090
4	MCI	Initial moisture content	0.125	0.270	0.310	0.360
5	MCF	Moisture content at field capacity	0.125	0.270	0.310	0.360
6	MCW	Moisture content at wilting point	0.063	0.135	0.155	0.180
7	PSI	Pore size index	0.398	0.220	0.250	0.168
8	Ψ	Soil matric potential, cm	205.7	111.5	280.9	291.6
No.	GW Zone	Description	Moraine	Complex	Till	Outwash
1	η_e	Aquifer effective porosity	0.175	0.270	0.310	0.360
2	K	Aquifer hydraulic conductivity, mm/h	30.5	12.4	4.67	6.35
Surface roughness parameters						
No.	Type of land use		Shallow		Deep	
1	Open Water		0.045		0.030	
2	Low Intensity Residential		0.020		0.011	
3	High Intensity Residential		0.015		0.011	
4	Commercial/Industrial		0.014		0.010	
5	Transportation		0.013		0.010	
6	Barren Land		0.100		0.050	
7	Deciduous Forest		0.198		0.184	
8	Evergreen Forest		0.198		0.184	
9	Mixed Forest		0.198		0.184	
10	Shrub/Scrub		0.200		0.100	
11	Grasslands		0.350		0.240	
12	Hay/Pasture		0.200		0.100	
13	Row Crops		0.180		0.100	
14	Woody Wetlands		0.060		0.045	
15	Herbaceous Wetlands		0.060		0.035	

* The soil zone A has the highest infiltration potential representing loamy sand, followed by soil zone B, which has moderately low runoff potential representing loamy silt. Similarly, soil zone C has slightly restricted vertical conductivity representing silty clay loam texture, followed by soil zone D, which represents clayey soil with a higher moisture content but low vertical conductivity. The four GW zones represent the unconsolidated aquifer systems that form the saturated subsurface for the UWR basin. The roughness parameters transition from shallow (maximum) to deep (minimum) based on an exponential decay function dependent on depth of flow.

threshold for merging cells and 25% threshold for unmerging cells as the WT moves upwards or downwards is provided to ensure continuity and consistency in the wetting and drying of cells in the vadose zone.

The volume of water available for infiltration at every time-step is calculated as the rainfall volume in that time plus the volume of water ponded on the surface minus the amount of evapotranspiration (ET). The potential evapotranspiration (PET) at every time-step is first removed from the rainfall volume and ponded water. In case the amount of PET required is higher than the rainfall and ponded water, the difference is extracted from the soil column available for ET (ground surface to root depth). The current soil moisture content in each cell is adjusted based on actual ET (AET) requirements before proceeding with the unsaturated vertical flow computations. The reference evapotranspiration (RET) in ICPR is calculated using the Penman-Monteith equation (Appendix A, Eq. (A.14)). The empirical equations provided in Allen et al. (1998) are used in conjunction with meteorological data to calculate the RET. Since the RET is calculated assuming the surface to be 'turf grass' in good condition, the RET is converted into PET using crop coefficients which can vary based on the crop-type, soil-type, and time of year. Evapotranspiration is not included in the first part of this study (described in Section 4) as it deals with event-based simulations. However, ET calculations are included for the continuous simulations presented in Section 5.4.

3.3. The saturated groundwater system

A finite element approach with a six-point quadratic triangular element as described by Martínez (1989) is used in ICPR to solve the continuity equation (Appendix B, Eq. (B.1)) for unsteady phreatic two-dimensional groundwater flow (Streamline Technologies, 2018). Nodes are placed at triangle vertices and midpoints along the triangle edges. Like the surface flow computational mesh, polygons are formed around the triangle vertices. Polygons are also formed around the triangle midpoints. This set of polygons is referred to as the subsurface honeycomb.

3.4. Integrating surface and subsurface systems

The surface and subsurface honeycomb meshes are simultaneously intersected with soils, land use and rainfall zone thematic polygon map layers (Fig. 3), forming a system of sub-polygons or soil cylinders. Each soil cylinder has a surface node, a groundwater node, as well as soil, land use and rainfall zone attributes. A portion of the rainfall may enter the soil column and flow vertically through the vadose zone. Water that does not enter the soil column is assigned to its respective surface node. Water is aggregated if multiple soil cylinders share the same surface node and then moved horizontally on the surface along triangle edges. Any water for a given soil cylinder crossing the interface between the vadose zone and the saturated zone is aggregated and delivered to its respective groundwater node. If the soil column becomes saturated and the surface is inundated, a known head condition is applied to the corresponding groundwater node based on the surface node stage. Seepage into or out of the groundwater system at that location is calculated by the groundwater model and removed from or delivered to the surface node.

3.5. Time marching scheme

The coupling sequence between the vadose zone, the surface hydraulics and the saturated groundwater system is as follows: (1) Start incrementing the hydrology clock (vadose zone); (2) Start incrementing surface hydraulics clock until it catches up to the hydrology clock; (3) If the hydrology clock is less than the groundwater clock plus groundwater time increment, go to step 1; and (4) Start incrementing the groundwater clock.

The hydrology (vadose zone) and groundwater time increments are static. The hydrology time increment is usually several minutes in duration whereas the groundwater time increment is typically an hour or longer. Hydrology runoff rates are saved at the beginning and end of a hydrology time increment and delivered to the appropriate surface node. Ponded water at the beginning of the hydrology time increment is applied across the full hydrology time increment. Groundwater recharge volume based on fluxes across the vadose zone–saturated zone interface is aggregated and delivered to the groundwater model at its time increment. The surface hydraulics time increment is typically in seconds or fractions of seconds in duration and operates between a user-specified minimum and maximum time increment.

There are two (2) time marching options in ICPR. The first option is a Successive Approximation technique with Over-Relaxation (SAOR). This is an iterative solution that solves for heads at nodes and flow rates along triangle edges. It has an adaptive time-step and changes between user-specified minimum and maximum time increments. However, a constant time-step is used throughout the computational mesh at a given point in time. Consequently, the time-step is typically driven by

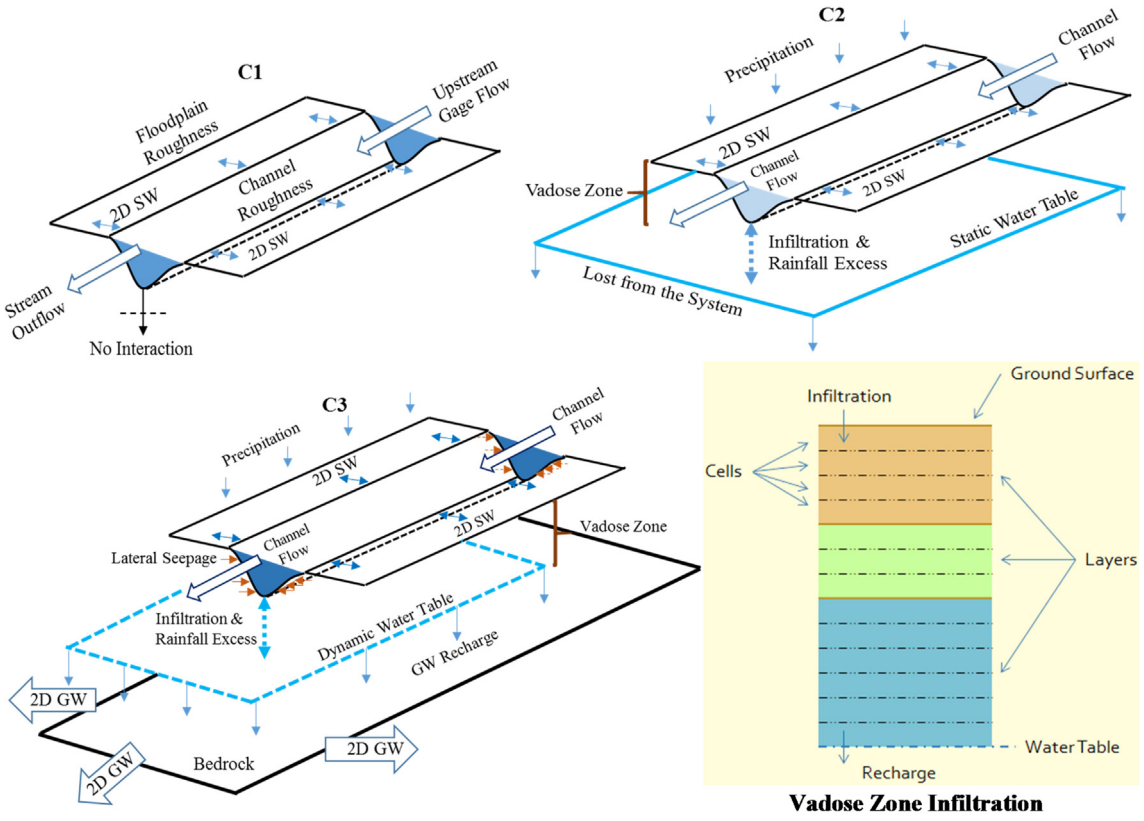

Fig. 4. Conceptual illustration of C1, C2, C3 and vadose zone infiltration.

the node with the least amount of storage.

The second option (used in this study) is based on a second order Runge-Kutta technique (modified Euler method) that varies the time-step not only in time, but also spatially (Domingues et al., 2008). It is referred to as the "FIREBALL" method in ICPR and is 2.5 to 30 times faster than the SAOR method for large projects (Streamline Technologies, 2018). The method involves establishing a set of time-step levels at the beginning of a simulation based on the minimum and the maximum calculation times, with each successive level doubling in duration. For example, if the minimum and maximum calculation times are set to 0.01 and 5.12 s, respectively, then ten (10) time-step levels are established, and routing calculations are based on these time-step levels. A maximum allowable time-step is then determined for each node based on inflows, outflows, and available storage, such that the change in stage does not exceed the user specified change in stage tolerance, which is typically set such that the mass-balance error is minimal. The time-steps are rounded down to the closest time-step level, following which, a pass is made through the entire network, beginning at nodes with the lowest time-step level, to ensure that the neighboring nodes do not increase more than one time-step level.

For example, if a total of ten (10) time-step levels are chosen, the inner-most level with the smallest time-step will be calculated 512 times compared to the outer-most level with the largest time-step, but the neighboring cells do not increase by more than one level. Once all cells on all time-step levels are calculated, the maximum allowable time-steps for all the nodes are re-evaluated and the process is repeated. A finite element time marching scheme is used for the groundwater model based on a quadratic shape function. The algorithm solves for heads at every node (triangle vertex and midpoint) in the computational mesh. In this study, the hydraulic routing time-interval is set between 0.01 and 5.12 s (ten time-steps), the hydrology is updated after every 300 s (5 min), and the groundwater flows, seepages and recharge rates are calculated at every hour (3600 s).

4. Methodology

The overall goal of this study is to show that an integrated SW-GW modeling approach provides more robust and accurate results compared to the conventional surface water modeling approach. This goal is accomplished by creating three modeling configurations (Fig. 4) by gradually increasing physical complexity to show the relative improvement in the model results. More details on these configurations, including the steps involved in creating them are provided below.

4.1. Creation of ICPR model configurations

4.1.1. Surface model discretization (C1)

The C1 model represents a 2D surface water model, which uses gage data at upstream USGS stations, and routes the water solely based on topographic variation and roughness characteristics. This configuration represents the default conventional approach to flood modeling driven by upstream discharge hydrograph. The elevation data for this model is obtained from the gridded 9 m resolution LiDAR. The river geometry for this configuration is defined using a flexible triangular mesh, such that it is dense in the channel and its floodplain (as shown in Fig. 3), and coarse for the land surface away from the river to reduce computation time. This flexible mesh structure ensures that the mass balance is simulated accurately where most of the water transport is taking place. The triangular mesh in ICPR is overlain on the LiDAR DEM and the elevation of LiDAR cell directly intersecting with a specific triangular vertex is extracted and assigned to the vertex. The flow hydrodynamics is simulated by using a 2D overland flow routing that is based on the solution of diffusive wave formulations (Appendix A, Eqs. (A.8)–(A.10)). Additionally, C1 does not require any additional hydrologic inputs (e.g. rainfall), since it has no subsurface connectivity, and is based solely on the traditional hydraulic routing techniques used for estimating flood depths and extent of inundation. Basically, the ground surface is assumed to be impervious for C1 and the streamflow

from eight upstream gages are routed without any rainfall, thereby representing a configuration that is synonymous to the traditional 2D surface water routing models such as HEC-RAS 2D and LISFLOOD-FP.

This triangular mesh for the 2D overland flow region is generated using the 'breakline' and 'breakpoint' feature in ICPR. The 'breakline' feature is a polyline shapefile generated by digitizing the river channels in the study area using aerial imagery and LiDAR data. Each point used to create the polyline 'breakline' feature is assigned a triangular vertex node in ICPR and the triangle edges are formed along the polyline. Therefore, the channel flow rates are computed along the triangle edges within the ICPR computational scheme. Since more points are required to digitize river bends, the resultant mesh is denser along the river bends and at confluences. Since the DEM resolution for the LiDAR data is 9 m, the 'breakline' feature is digitized such that the minimum distance between any two vertices is 9 m and the maximum edge length along straight channels is 27 m. Therefore, the average triangular edge length in the river channels is 15 m. For mesh digitization outside the river channels, the 'breakpoint' feature, which is a point shapefile, is used for mesh generation. Every point in the 'breakpoint' shapefile is assigned a triangular vertex in the mesh and these features can be automatically generated in ICPR at a specified distance (for more information on breakpoints and breaklines, please refer to, Streamline Technologies, 2018). Using this principle, triangular 'breakpoint patterns' with an average edge length of 60 m and 300 m are assigned inside and outside the floodplain respectively.

4.1.2. Subsurface model discretization (C2 and C3)

The overland flow in C1 configuration is modified to include two subsurface configurations. In the first modification, referred to as C2, the overland flow can only interact with the unsaturated soil layer (vadose zone) with a static WT. The vadose zone thickness is determined using gSSURGO data for the region, which remains constant throughout the simulation. The C2 configuration is like other commonly used hydrologic models such as HEC-HMS and SWAT that route the rainfall excess surface flow and the water percolating beyond the vadose zone is lost as aquifer recharge. The initial soil moisture in the vadose zone is assumed to be equivalent to field capacity at the beginning of the simulation. As mentioned in Section 3.2, the water movement in the vadose zone, and subsequent GW recharge is computed using the refined Green-Ampt method (Streamline Technologies, 2018). A total of twenty-five cells are used for the vadose zone in this study. Initially, all the cells start with the same parameters as shown in Table 2, but the moisture content across each cell can vary with time as the fluxes through each individual cell are tracked in both upward and downward directions. During the simulation at each time-step, the wetting front moves through individual unsaturated cells, which are wetted or dried using the available soil storage and unsaturated hydraulic conductivity. Fig. 4 provides an illustration of the vadose zone discretized into multiple cells which are used to redistribute the soil moisture.

In the third configuration, referred to as C3, the WT in C2 is made dynamic so the water that percolates beyond the vadose zone is used to increase the storage in the surficial aquifer, which results in the rise of the WT. Similarly, during dry conditions, the WT recedes and increases the vadose zone depth. Along with vertical movement of the WT, C3 also incorporates GW contributions from horizontal gradients causing seepage fronts that discharge into the Wabash River. Within the subsurface in C3, the GW recharge rates from the vadose zone for a given WT elevation are converted to a volume, which is based on the hydrological computational time increments. This volume in-turn determines the change in the WT elevation for the next time increment.

To simulate the GW dynamics in C3, an initial WT surface is required at the beginning of the simulation. To generate this surface, first, the WT depth contours obtained from IDNR's potentiometric surface maps are interpolated using the inverse distance weighting (IDW) method to form a WT depth raster at a spatial resolution of 30 m. Second, this WT depth raster is subtracted from the ground LiDAR (resampled to 30 m) to obtain a WT elevation surface. Third, this surface is imported into an initial version of the C3 model, which is then simulated at steady-state for one month using the daily average streamflow for the streams in the watershed. Finally, it is assumed that the WT surface reaches equilibrium at the end of this steady-state simulation. The WT surface obtained at the end of the steady-state simulation is used as the initial WT surface for the C3 model used in this study.

Within the surficial aquifer, the GW flow is calculated using the 2D unsteady phreatic solution of the continuity equation using a finite element formulation. More specifically, a six-point triangular element is used with a quadratic interpolation function, and the system of equations is solved using the Cholesky method (Kuiper, 1981; Martínez, 1989). A 2D subsurface discretization also allows C3 to account for the non-uniform distribution of the hydraulic properties in the vadose zone and surficial aquifer (Kollet and Maxwell, 2006). Since the GW processes operate at larger spatial scales compared to SW processes (Bloschl and Sivapalan, 1995; Wood et al., 1988), a coarser resolution mesh, with an average edge length of 45 m in the channel, 240 m in the floodplain, and 900 m outside the floodplain, is created. A detailed description of the modification of the continuity equation for finite element formulation is described in Appendix B and can also be accessed from ICPR's Technical Reference Manual (Streamline Technologies, 2018).

Table 2 presents the uncalibrated Green-Ampt parameters used for C2 and C3, and surficial aquifer parameters used for C3, that are classified based on soil zones and the type of aquifer system respectively. The gSSURGO database contains spatially distributed hydrologic soil group classification based on runoff potential and the four soil zones used in this study are based on this classification. The saturated vertical conductivity, moisture content at field capacity, and at wilting point (presented in Table 2) reflect the median values of the specific soil zones in the gSSURGO database. The other parameters require information on the soil texture percentages, which are also available from the gSSURGO database. Using the soil texture percentages, and the equations provided in Rawls (2004), the other subsurface parameters such as pore size index, soil matric potential, and residual moisture content are evaluated (Streamline Technologies, 2018). For the GW zones, the map of the spatial distribution of different unconsolidated aquifer systems for Indiana is available from IGIC's Indiana Map Server (http://maps.indiana.edu/index.html). The aquifer properties for Wabash Valley are obtained from a study on the investigation of groundwater resources in Indiana (Pohlmann, 1987).

4.2. Model simulations using three configurations

The three configurations are run in an unsteady-state to simulate hourly streamflow, stage and extent of inundation for a month from April 11th, 2013 to May 10th, 2013. During this period, multiple rainfall events of varying magnitude were observed in Indiana that resulted in a peak streamflow corresponding to a 50-year return period in the Wabash River at Lafayette. The first 5 days of simulation are used for model initialization, which is completed when all the models reach equilibrium and all reaches are connected. The equilibrium is reached when the mass balance error in the system stabilizes to a value less than 1%. The outputs from the three model configurations are compared with observed data for the next 25 days at the watershed outlet. A period of 25 days is chosen to simulate both high and low flow conditions that occurred during and after the storm event, respectively. Evapotranspiration is not included in C2 and C3 during the one-month simulation based on the assumption that the effect of ET would be negligible during a short and extremely wet period.

The input parameters are kept unchanged for different model configurations because the goal is to investigate the sensitivity of flood simulation from the three configurations to subsurface flow integration

under normal climatic conditions. It should also be noted that the model comparisons are based on uncalibrated parameter inputs because calibration can result in unrealistic representation of relative contributions from the overland and subsurface processes due to the existence of equifinality (Pappenberger et al., 2005; Beven, 1993). After applying the three models to simulate the one-month period, the streamflow, stage, and extent of inundation are evaluated and compared between models. The stage is evaluated by subtracting the channel bed elevation at the gage from the WSE. The stage is used instead of WSE as WSE is a scale-dependent parameter, which can create bias in the results due to the elevation (or altitude) of the location. The relative performance of these models is also evaluated by comparing the simulated results with observed data.

4.3. Statistical comparison of model configurations

In order to evaluate the goodness of fit between the three configurations and observed data, the coefficient of determination (R^2) is calculated. While R^2 is used as a measure of linear trend, the Nash-Sutcliffe Efficiency (NSE, Nash and Sutcliffe, 1970) which reflects the overall fit of a hydrograph, is also evaluated. Similarly, the slope parameter, which provides a measure of overprediction or underprediction of model outputs with increasing magnitude, is evaluated. In addition, Percent Bias (PBIAS, Sorooshian et al., 1993), a statistic used to measure if the average tendency of simulated data is larger or smaller than observed data, is also calculated (Gupta et al., 1999). Finally, the RMSE-observations standard deviation ratio (RSR), which is a scaled-normalized parameter, is evaluated to estimate the variation in model residuals.

4.4. Spatial aggregation and computational performance of model configurations

As mentioned in Section 3, the ICPR model uses a flexible spatiotemporal structure for the surface and GW regions. The application of flexible resolution spatial mesh and variable hydraulic time-steps (0.01 to 5.12 s) significantly improves the computational efficiency of these models for large watersheds. Table 3 presents the spatial aggregation parameters of the surface and GW meshes (provided in parenthesis for C3) generated for the UWR basin (Fig. 3). Since the same surface mesh is used for the three configurations, the number of triangles and the mean triangular area is the same. To compare the spatial resolution of triangulated irregular networks (TINs) with gridded DEMs, Vivoni et al. (2005) used two spatial aggregation parameters, the horizontal point density (d) and the equivalent cell size (r_e), which can be evaluated using Eqs. (1) and (2).

$$d = \frac{n_t}{n_g} \tag{1}$$

$$r_e = \sqrt{\frac{A}{n_t}} \tag{2}$$

where, d = horizontal point density; n_t = number of triangular nodes (or vertices); n_g = number of DEM nodes; r_e = equivalent cell size (or length scale); and A = basin area. The number of DEM nodes (n_g) are evaluated using the 9 m LiDAR for the surface region and the 30 m initial WT raster for the GW region. The 'r_e' values for the surface (156 m) and GW (428 m) meshes represent the equivalent spatial resolution of the TINs used in this study. Similarly, the 'd' values provide a ratio of the number of computational elements used in the surface (0.003) and GW (0.004) meshes in comparison to the fixed-resolution gridded DEMs.

Table 3
Spatial aggregation and computation performance of C1, C2 and C3.

Computational Elements	C1	C2	C3
Number of triangles in the mesh	392,148	392,148	392,148 (43,509)
Mean triangular area (km^2)	0.015	0.015	0.015 (0.134)
Equivalent cell size, r_e (m)	156	156	156 (4 2 8)
Horizontal point density, d	0.003	0.003	0.003 (0.004)
Build time (hours)	1.5	1.5	3.3
One-month simulation time (hours)	15.5	16.1	24.9

The models used in this study are simulated on a 4-core Intel i-7 system with a processing speed of 3.7 GHz. The 'build' process involves generation of the meshes required for simulation, intersection of all input datasets to extract model parameters, and assignment of nomenclature to mesh nodes and vertices. As shown in Table 3, the 'build' and 'simulation' times for C1 and C2 are very similar, as the hydrodynamic processes control the total simulation time for both configurations. The 'build' and 'simulation' times for C3 are 120% and 60% longer than C1. Although C3 requires a longer computational time, the computational efficiency of C3 can be increased significantly by increasing the number of simulation cores as the SW and GW regions can be parallelized in ICPR. Even without parallelization, a one-month simulation can be completed in approximately one day, highlighting the overall computational efficiency of the flexible spatiotemporal structure used in this study.

5. Results and discussion

The results are presented in four parts: (i) comparison of the three model configurations (C1, C2 and C3); (ii) quantification of the relative contribution of watershed processes during flooding; (iii) evaluating the effect of antecedent soil conditions on flood outputs; and (iv) further validation of results by applying C3 under different flow and watershed conditions

5.1. Comparison of the three model configurations

5.1.1. Comparison of model outputs with observed data

In this section, the observed streamflow and stage is compared with the simulated streamflow and stage for C1, C2, and C3, respectively. It should be noted that all the models begin from the same initial surface storage, and C1 does not have any infiltration into the soil column. The results presented in Fig. 5a show that C1 overpredicts the streamflow significantly near the peak and underpredicts during low flows. This result suggests that the surface water models produce higher outflow during flood events as the water flowing into the surface system (inflow) is fully recovered as either surface storage or outflow. Since the inflow volume in C1 is not removed from the surface system due to the absence of processes like infiltration, evapotranspiration, GW seepage and recharge, the resulting outflow volumes are higher for C1. On the other hand, C2 severely underpredicts the streamflow during low flow conditions, but predicts the peak streamflow accurately when compared to observed data. While a portion of the infiltrated water is stored in the vadose zone and some is delivered to the surface as excess runoff in C2, most of the water exits the system by percolating out of the vadose zone and is lost as subsurface recharge, resulting in an underprediction in C2. Due to a better physical process representation, C3 performs well in predicting the streamflow for the entire duration of the simulation. Fig. 5b suggests that C1 fails to predict the stage accurately for the duration of the simulation. In comparison to streamflow, the error in estimating stage for all models is less severe near the hydrograph peak, because the stage is more resistant to fluctuations in streamflow when the water inundates outside the main channel and into the floodplain, causing a significant increase in the flow area. Additionally, a change in streamflow can also affect the flow velocities, resulting in a less severe impact on stage. The scatterplots about the line Y = X shown in Fig. 5c and d further highlight the overall accuracy of C3 in estimating streamflow and stage.

The streamflow and stage hydrographs for the three configurations

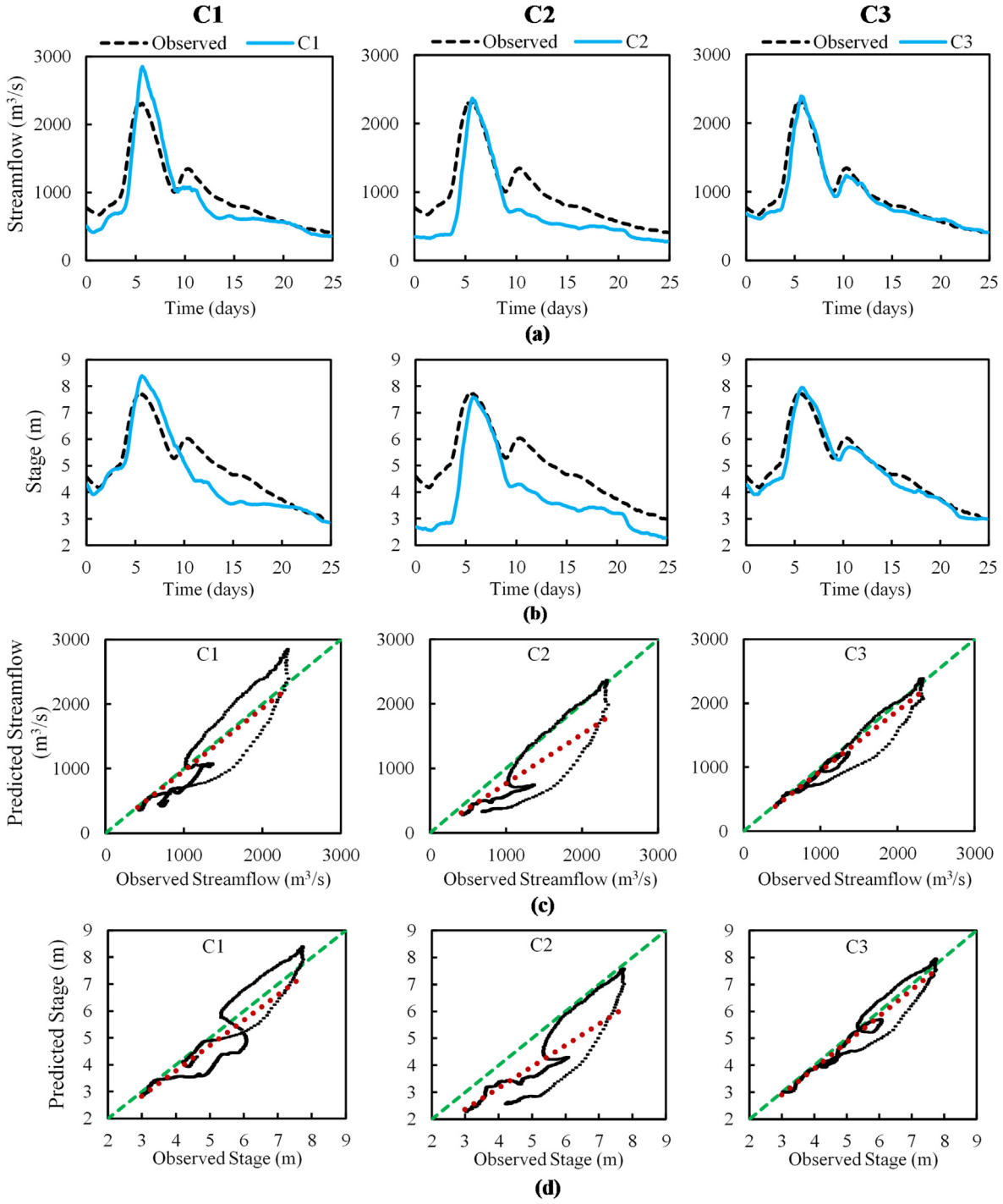

Fig. 5. (a) Streamflow hydrographs at the outlet; (b) stage at outlet gage station; (c) streamflow scatterplots; and (d) stage scatterplots for C1, C2, and C3 for a 25-day simulation (April 16th to May 10th, 2013).

highlight the importance of including a dynamic WT and a variable vadose zone thickness. In the context of streamflow generation, current hydrologic models such as HEC-HMS and SWAT, are severely limited in considering this dynamic nature. To improve the prediction using such models, the parameters need to be calibrated to produce a best-fit combination of parameters (Arnold et al., 2012; Zhang et al., 2013). However, this process of calibration does not guarantee model performance during different hydrologic and climatic conditions (Liew et al., 2005; Schuol and Abbaspour, 2006). Assuming a fixed vadose zone thickness can also restrict the maximum volume of water available to plants in the root zone which, in turn, may influence other processes such as evapotranspiration, which is a dominant variable during normal climatic conditions. Here, C2 represents hydrologic models that do not account for groundwater movement, and therefore, underpredicts the streamflow and stage. C3 includes a dynamic WT along with the surficial aquifer characterization, which significantly improves the prediction. The C3 outflows suggest that the total amount of water infiltrating into the subsurface reduces on inclusion of a dynamic WT. Additionally, a fraction of the water is also recovered from the subsurface in the form of seepage due to the direct interaction of the WT with the surface, which contributes towards a more accurate low flow estimation.

Table 4
Comparison of model performance for peak and lowest streamflow.

Condition	Variable	Observed	C1	C2	C3
Peak	Streamflow (m^3/s)	2317.0	2850.8 (+23.0)	2369.0 (+2.2)	2389.3 (+3.1)
	Stage (m)	7.71	8.39 (+8.9)	7.58 (−1.7)	7.93 (+2.9)
	Inundation Area (km^2)	NA	171.4	155.1	188.2
Lowest	Streamflow (m^3/s)	411.3	355.4 (−13.6)	278.1 (−32.4)	406.8 (−1.1)
	Stage (m)	2.99	2.87 (−4.1)	2.27 (−24.1)	2.99 (−0.2)
	Inundation Area (km^2)	NA	119.4	106.3	118.9

*The values in parenthesis represent the relative error (%) with respect to observed data.

Even though C2 has a better physical process representation than C1, its performance is worse than C1, as shown in Table 4 and Fig. 5. These results suggest that a fixed vadose zone model that permits water percolation into an infinite GW region, without properly quantifying recharge and WT location, performs worse than simply using a model with an impervious surface (C1). To improve the performance of models like C2, it may be more beneficial to restrict the percolation out of the unsaturated zone by assuming an impervious bottom soil layer, thereby, providing a fixed storage in the soil system. This modification can reduce the underprediction in C2, as it may improve the simulation of Hortonian runoff (infiltration excess), even though Dunne runoff (saturation excess) may not be simulated accurately without proper conceptualization of GW processes (Xie et al., 2003). For events that are primarily affected by Hortonian runoff, the error induced by excluding GW processes may be offset by incorporating an unsaturated zone without GW recharge. However, several factors can result in Hortonian-runoff-dominated events across watersheds, for example, the spatial heterogeneity in soil properties, antecedent soil conditions, watershed topography, and rainfall intensity. Therefore, before choosing a model configuration like C2, these factors should be considered, otherwise, the results may not be accurate without GW incorporation, as shown in this study.

Fig. 6 shows the WSE and top width for the three configurations at a cross-section just upstream of the outlet. The results from C2 suggest that there is no inundation in the floodplain, and the water remains inside the main channel for the lowest flow, however, both C1 and C3 suggest inundated floodplains near the outlet. The top width and WSE at low flows are similar for both C1 and C3. The top width across the channel for peak flow is highest for C1, whereas, the difference between C2 and C3 is not as appreciable when compared to low flows. A higher top width for C1 during peak flow is representative of higher outflow volumes as shown in Fig. 5a, and a smaller top width during low flows is indicative of the underprediction by C2.

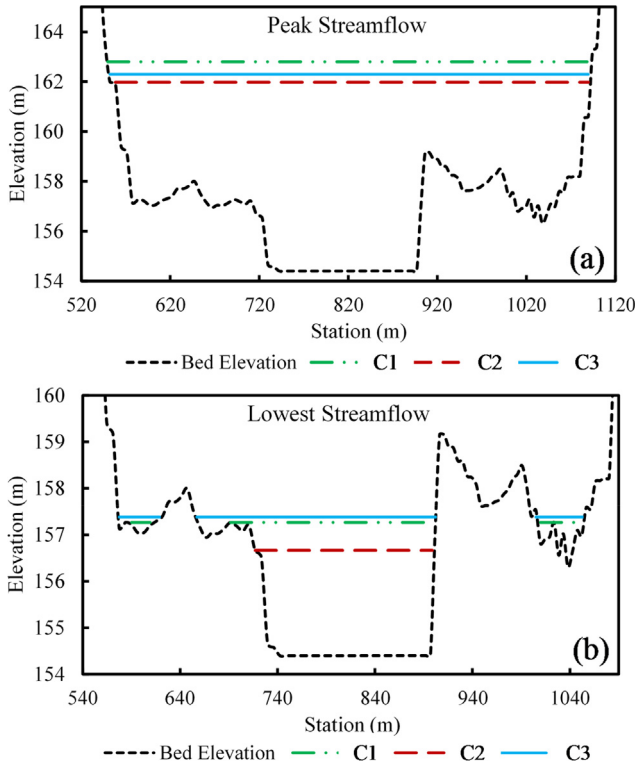

Fig. 6. Cross-sectional profiles for C1, C2 and C3 for (a) peak streamflow and (b) lowest streamflow.

Fig. 7 presents the flood inundation maps near the Wabash-Tippecanoe confluence for the highest (peak) and lowest streamflow during the simulation. The difference in the location and magnitude of inundation between the three models is evident from the flood maps at peak streamflow (Fig. 7a–c). For C2, the inundation area measured at both peak and lowest streamflow is significantly lower (Fig. 7b and e) than C1 and C3. As shown in Table 4, the peak flow flood inundation area is smallest for C2 (155.1 km^2), followed by C1 (171.4 km^2) and C3 (188.2 km^2). Overall, C3 has the highest flood inundation extent since it accounts for surface ponding during extreme rainfall as the subsurface becomes saturated. Additionally, water seeping laterally from the rivers into the subsurface can seep out elsewhere causing ponding. Therefore, C3 can capture river-floodplain interactions across both the surface and subsurface regions. In contrast, C1 only shows inundation due to riverine flow that inundates into the floodplain, and hence, the flooding is localized around the river channel. The flood inundation area corresponding to the lowest flow for C1 (119.4 km^2) and C3 (118.9 km^2) are approximately equal, which suggests the traditional surface water routing approach and the integrated approach produce similar results during low flows, when the water remains inside the river channels.

The results presented in this section suggest that the overall model performance for C3 is superior when compared to C1 and C2. However, the extent of inundation does not depend only on streamflow and stage, but also on the accuracy of topographic data. In this study, the extent of inundation estimated by the model configurations is not compared with observed flood inundation, and therefore, it is essential to note that the flood inundation maps presented here only provide a relative difference between the model configurations. From a watershed perspective, if the inflow and outflow from the watershed is predicted accurately, the extent of inundation will be a function of the resolution and vertical accuracy of topographic data.

5.1.2. Statistical comparison of model performance

Fig. 5 suggests that C3 performs best when compared to observed flow, however, it is essential to evaluate model performance statistics to further validate these conclusions. Table 5 presents the statistical parameters for evaluating goodness of fit between the three models and observed data. The statistical performance of the models in estimating streamflow suggests that C3 (R^2 = 0.95) performs best, followed by C1 (R^2 = 0.85), and C2 (R^2 = 0.80). As mentioned earlier, the stage is evaluated by subtracting the bed elevation from the WSE at the outlet. The model performance in estimating stage suggests that C3 has a high R^2 value of 0.95, but both C1 and C2 have a diminished performance

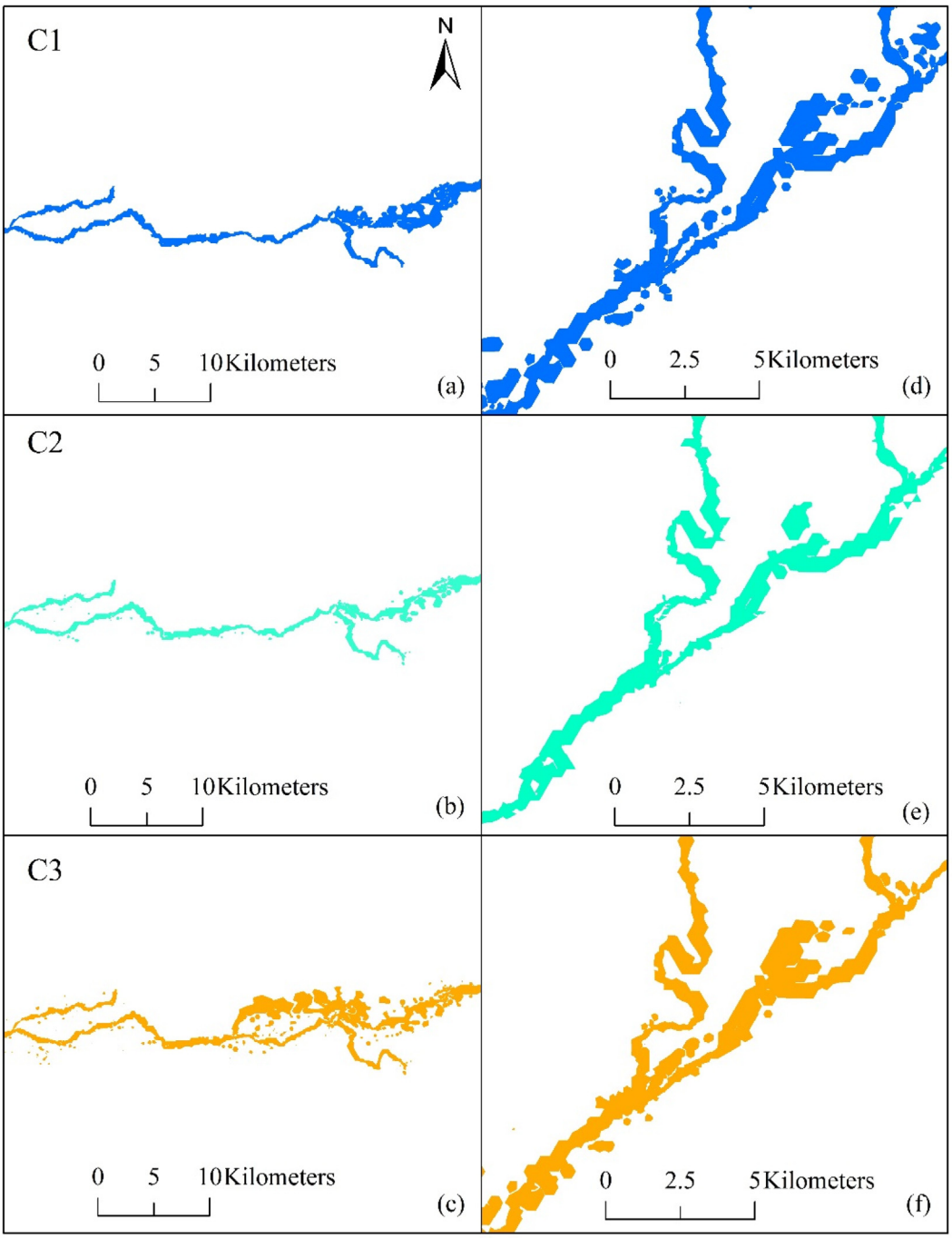

Fig. 7. Flood inundation maps across two locations for (a) C1 peak streamflow; (b) C2 peak streamflow; (c) C3 peak streamflow; (d) C1 lowest streamflow; (e) C2 lowest streamflow; and (f) C3 lowest streamflow.

with R^2 values of 0.81 and 0.78 respectively. A very low NSE for C2 in estimating streamflow and stage indicates an unacceptable performance (Moriasi et al., 2007). Even though C1 and C3 have comparable R^2 values, high NSE values of 0.94 and 0.93 in estimating streamflow and stage clearly suggest that C3 has a very good performance when compared to observed data, based on the model evaluation guidelines by Moriasi et al. (2007).

While both C1 and C3 underpredict the rising limb of the hydrograph, the overall slope in comparison to the line Y = X is close to 1 which indicates that neither of the models are consistently overpredicting or underpredicting the streamflow. Overall, C3 performs better statistically in estimating streamflow highlighted by a lower PBIAS (−6.0%) compared to C1 (−8.6%). Similarly, C3 also has a better performance in estimating stage as shown by a very low PBIAS (−3.2%) compared to C1 (−6.6%) and C2 (−22.4%). A low slope (0.77) for C2 indicates that the model underpredicts the streamflow consistently, even though the relative error in peak streamflow (Table 4) is very small (+2.2%). In addition, C3 has a lower RSR when compared to C1 and C2, which further highlights the improvement in model performance due to an accurate representation of physical processes.

Since an inaccurate mesh resolution can cause mass balance errors in the model, the performance of the three configurations is tested for two additional mesh resolutions, including one that is coarser and

Table 5
Statistical analysis of model performance.

Streamflow at Outlet					
Model	R^2	NSE	Slope	PBIAS	RSR
C1	0.85	0.77	0.96	−8.6	0.47
C2	0.80	0.50	0.77	−28.8	0.70
C3	0.95	0.94	0.95	−6.0	0.24
Stage at Outlet					
Model	R^2	NSE	Slope	PBIAS	RSR
C1	0.81	0.69	0.94	−6.6	0.56
C2	0.78	0.01	0.79	−22.4	0.99
C3	0.95	0.93	0.97	−3.2	0.26

another that is finer than the one presented in this study. The overall conclusions did not change, but the degree of improvement compared to the observed data was different when using a coarser mesh resolution. For example, the reported R^2 values when using a coarser mesh resolution for C1, C2 and C3 are 0.59, 0.76 and 0.85 respectively, and therefore, the integrated model performed better regardless of the mesh resolution. Using the mesh resolution finer than the one used in this study did not provide any additional improvement in the results for any configurations.

5.2. Quantification of the relative contribution of watershed processes

The results in the previous section signify the importance of integrating rainfall and subsurface flow with surface water models for production of flood inundation maps. C3 is uncalibrated and yet the performance statistics suggest that this model predicts both the streamflow and stage accurately for the simulation period. In addition to reducing calibration uncertainty, it is also essential to quantify the contributions from different watershed processes during flood events. This analysis can help in highlighting which process plays a dominant role in exacerbating or attenuating the flood responses.

To quantify the relative contribution of different processes during a storm event, the volumetric contributions from hydraulic routing, vadose zone, and GW recharge, are evaluated for C3. Since estimating the exact flow paths for GW flow regimes is beyond the scope of this study and is less relevant in the context of flood prediction, the volumetric contribution divided by the watershed area (mm), is used as a metric for quantifying the relative contributions from different physical processes. Fig. 8a presents the streamflow hydrograph for C3, which is used as a metric to evaluate the volume of water leaving the watershed through the surface. Fig. 8b shows the 'Stream Inflow', which is the cumulative volumetric inflow into the model from all eight upstream USGS gage stations for C3, and the 'Stream Outflow', which is the cumulative volume of water discharging or leaving the system from the model outlet, which is located at USGS gage 03335500, Wabash River at Lafayette. Fig. 8b also presents 'ΔSurface Storage', which provides a cumulative estimate of the increase or decrease in the surface water volume in the river-floodplain system for the entire watershed. When flood responses are mapped without rainfall and subsurface integration, (for example, C1), the difference in 'Stream Inflow' and 'Stream Outflow' should represent the change in surface water inundation for the watershed. For C3 on the other hand, the 'ΔSurface Storage' is also a function of rainfall excess and GW seepage.

Fig. 8c shows 'Precipitation', which is the cumulative rainfall for the entire drainage area during the entire simulation period. The 'Rainfall Excess' (shown in Fig. 8c) represents the hourly excess rainfall volume which is delivered to the surface as runoff from the vadose zone, after evaluating infiltration and initial abstraction losses. Therefore, this represents the volume of runoff per hour that causes surficial ponding and subsequent inundation. The 'GW Recharge' (shown in Fig. 8d) represents the volume of water removed from the vadose zone due to downward percolation, which is delivered to the groundwater system as recharge. In addition, when the WT rises and intercepts the surface, the water is discharged to the surface system as 'Lateral Seepage', shown in Fig. 8d. Therefore, both 'Rainfall Excess' and 'Lateral Seepage' contribute additional volume to the surface system during flood events, thereby resulting in increased flood inundation, which is highlighted in Table 4 and Fig. 7.

The hydrograph in Fig. 8a highlights that C3 can capture streamflow variability throughout the simulation. On the other hand, in addition to the overprediction near the hydrograph peak, C1 underpredicts streamflow after a simulation time of 220 h, as highlighted in Fig. 5a. As shown in Fig. 8d, the subsurface storage increases significantly during peak rainfall intensity, which accounts for reduction in overall surface storage, thereby producing a more accurate streamflow prediction during high flow conditions. After the rainfall event, the vadose zone storage recedes resulting in more GW recharge. This increase in potentiometric head in the surficial aquifer causes increased lateral seepage (Fig. 8d) from the subsurface into the river system. This lateral seepage volume results in a more accurate streamflow prediction during low flow conditions for C3 (after 400 h, as shown in Fig. 8a) when compared to C1, which does not capture the increased streamflow due to GW seepage. Therefore, subsurface processes influence both the streamflow, and the surface water inundation, throughout the simulation.

These results further highlight the shortcomings of the current surface water models that route the streamflow solely based on roughness coefficients. While C1 overestimates the streamflow for this watershed, the absence of subsurface processes can lead to an underprediction of streamflow in GW-dominated watersheds. To rectify this overprediction/underprediction in streamflow, modelers calibrate the roughness coefficients for decreasing/increasing the flow velocities, thereby, changing the volume of water intercepted in the surface system. This practice of calibrating often improves the model results for specific events, however, without a true representation of the streamflow attenuation or amplification caused by subsurface processes, these models can produce erroneous flood estimates for other events (Moore and Doherty, 2005).

5.3. Evaluating the effect of antecedent soil conditions on flood outputs

The results from the previous sections highlight the influence of subsurface processes on flood responses. The analysis in this section aims to evaluate the potential of existing vadose zone moisture content and WT location in controlling surface water inundation and streamflow generation. Therefore, only the subsurface component of C3 is modified in this step. The hypothesis is that the WT location determines the control of groundwater in redistributing soil moisture upwards in the vadose zone, which further impacts the land surface inundation. Three soil moisture scenarios are used to represent dry, moderate and wet conditions. For the dry scenario (D), the initial soil moisture in the vadose zone is near wilting point and the average depth of WT is approximately 6 m. Floods occurring during this scenario are synonymous to heavy rainfall occurring when dry conditions have existed for a long time before the event. Similarly, for the wet scenario (W), the vadose zone is very shallow (depth to WT < 0.5 m), and the degree of saturation in the vadose zone ranges between 0.90 and 0.95. Therefore, even a small amount of percolation can saturate the vadose zone as the initial soil moisture is very close to the porosity. Flooding in this scenario is synonymous to two extreme rainfall events occurring one after the other. The moderate scenario (M) represents the case where the soil moisture is at field capacity, and the WT is at an intermediate depth of 1.5 m from the surface, which also represents the NRCS's average vadose zone depth of 150 cm. The initial stage surface is imported from C3 using the stage outputs just before the 50-year storm event. The three scenarios (D, W and M) are run in an unsteady-state to simulate hourly

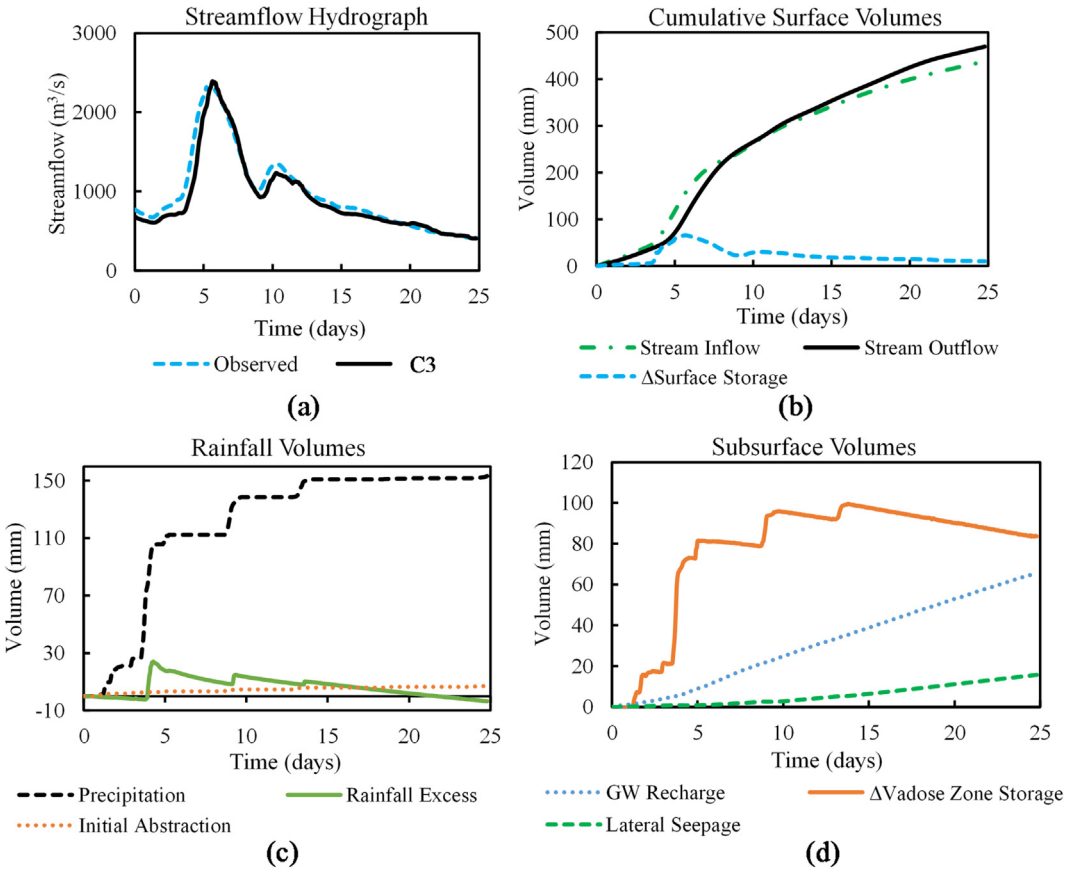

Fig. 8. (a) Streamflow hydrograph; (b) cumulative surface volumes; (c) volumetric contributions from rainfall; and (d) volumetric contributions from the subsurface for a 25-day simulation (April 16th to May 10th, 2013).

flood inundation and streamflow outputs for the storm event and the comparisons are used to analyze the influence of existing subsurface conditions on flooding.

The results in Table 6 suggest that there is a significant difference in both the streamflow outputs and inundation area obtained using the three scenarios. The M scenario is considered as the base model to evaluate the relative difference when dry and wet conditions exist. Table 6 also shows that there is a 10.8% increase and a 3.7% decrease in peak streamflow for W and D respectively. In addition, the flood inundation area obtained using D is less severe (−12.2%) due to completely dry subsurface conditions, and more severe (+40.5%) due to completely saturated subsurface conditions for W as shown in Fig. 9. For the same amount of precipitation, the cumulative change in vadose zone storage (Fig. 9c) is highest for D, followed by M, and lowest for W. Since W has a nearly saturated vadose zone, a larger portion of the rainfall is redistributed to the surface as excess rainfall, which directly affects the peak inundation area (Table 6). Additionally, this also results in significantly higher GW recharge volumes throughout the simulation for W. Therefore, when the subsurface is saturated, the peak streamflow, cumulative outflow volume and GW recharge, increase substantially.

Table 6
Hydrologic and hydraulic outputs for multiple antecedent soil conditions*.

Variable	Moderate (M)	Dry (D)	Wet (W)
Peak Streamflow (m^3/s)	2389.3	2302.1 (−3.7)	2647.8 (+10.8)
Lowest Streamflow (m^3/s)	606.8	394.2 (−35.0)	607.0 (+0.03)
Average Streamflow (m^3/s)	1204.6	997.5 (−17.2)	1294.7 (+7.5)
Peak Inundation Area (km^2)	188.2	165.2 (−12.2)	264.5 (+40.5)

* The values in parenthesis represent the relative difference (%) with respect to moderate (M) configuration.

The flood inundation maps presented in Fig. 9e–g represent the extent of inundation across the three configurations at the exact instance of time when the peak streamflow is observed at the outlet. The flood inundation map shown in Fig. 9g suggests that the extent of inundation at peak streamflow also increases when saturated conditions (W) exist, as there is no infiltration into the subsurface, in addition to higher GW contributions due to lateral seepage when the WT interacts with the surface. It should be noted that these instantaneous maps do not show the maximum inundation in the watershed during the simulation period which can even occur before or after the peak streamflow is observed. As shown in Table 6, there is only a 3.7% difference in the peak streamflow for the dry and moderate conditions. Therefore, when the peak streamflow is observed, there is very small difference in the extent of inundation between the dry and moderate configurations as shown in Fig. 9e and f. However, Table 6 suggests that there is an overall difference of 12.2% in the maximum inundation area between the two configurations suggesting that the maximum inundation at specific locations may have occurred at different times. The results validate the hypothesis that the location of the WT and existing soil moisture influence the overall flood inundation outputs.

The hypothetical phenomenon presented here using the W scenario highlights the potential of a fully saturated subsurface in increasing flood risk, which was observed during both Hurricane Frances and Hurricane Matthew (Weaver et al., 2016). Generally, floods corresponding to a specific return period have a standard map with a fixed extent of inundation, for example, 100-year FIRMs. However, due to existing saturated conditions, flooding from a 100-year flood event can be more severe than anticipated. Therefore, static flood maps should also be created based on antecedent soil moisture conditions as well as the WT location. For coastal aquifers that are prone to hurricane-

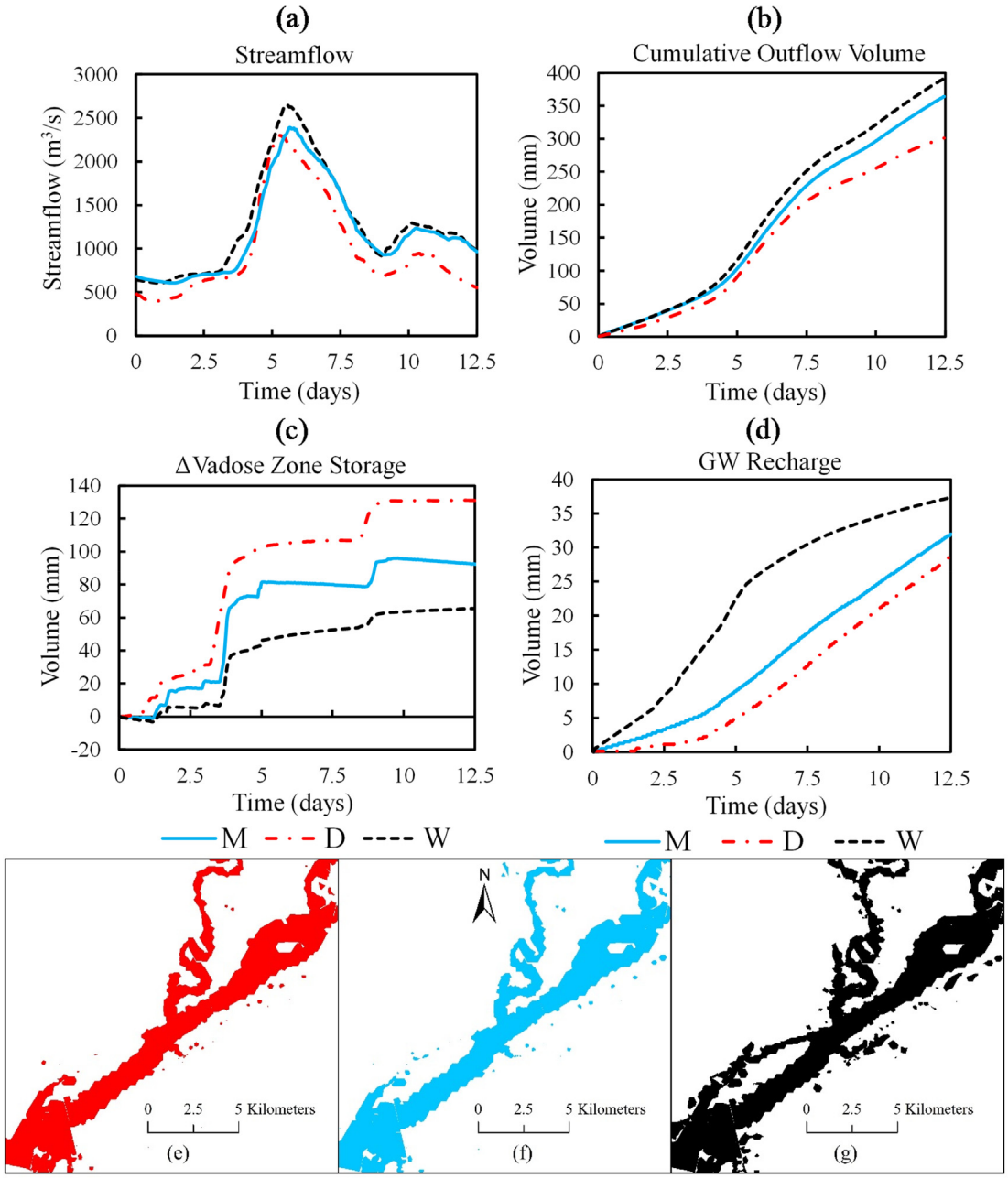

Fig. 9. (a) Streamflow at outlet; (b) cumulative outflow volume through the outlet; (c) cumulative change in vadose zone storage; (d) cumulative GW recharge; and flood inundation maps at peak flow for (e) dry (D); (f) moderate (M); and (g) wet (W) subsurface conditions for 12.5 day simulation (April 16th to April 28th, 2013).

induced rainfall, containing a shallow WT, and a higher antecedent soil moisture, these flood maps should be re-evaluated using integrated models so that the true flood risk can be estimated.

5.4. Further validation of C3 model

The results from the previous sections highlight the advantage of integrating hydraulic and hydrologic processes for simulating flood responses. To validate these findings, and further analyze the difference in the existing flood modeling approach (C1) and the integrated modeling approach (C3), two models for the UWR basin (referred to as C1-UWR and C3-UWR) are simulated for a long-continuous three-month period from February 15th to May 15th, 2018, using the same model parameters. The first two days are used as warm-up period and the results are compared against observed data at the outlet (Wabash River at Lafayette) from February 17th to May 15th, 2018.

The results shown in Fig. 10 and Table 7 clearly highlight the advantage of using an integrated modeling approach for flood prediction. The hydrograph in Fig. 10c highlights that C3-UWR can capture streamflow variability throughout the simulation, which can be seen from the superior NSE (0.97), PBIAS (−4.2%) and peak flow error (−5.3%). On the other hand, C1-UWR (Fig. 10a) overpredicts the streamflow for high and moderate flows throughout the simulation, which is highlighted by the NSE (0.92), PBIAS (+12.1%), and peak flow error (+14.9%). Additionally, the results from Figs. 5 and 10 suggest that both C1 and C3 can capture the low flows accurately. The accurate performance of C1 during low flows in streamflow-dominated streams like the Wabash River highlights its applicability in conditions where the water remains inside the river channel and the volume of water exchanged between the river and subsurface is insignificant in comparison to streamflow. Finally, the results also validate the applicability of the refined Green-Ampt method used in this study for

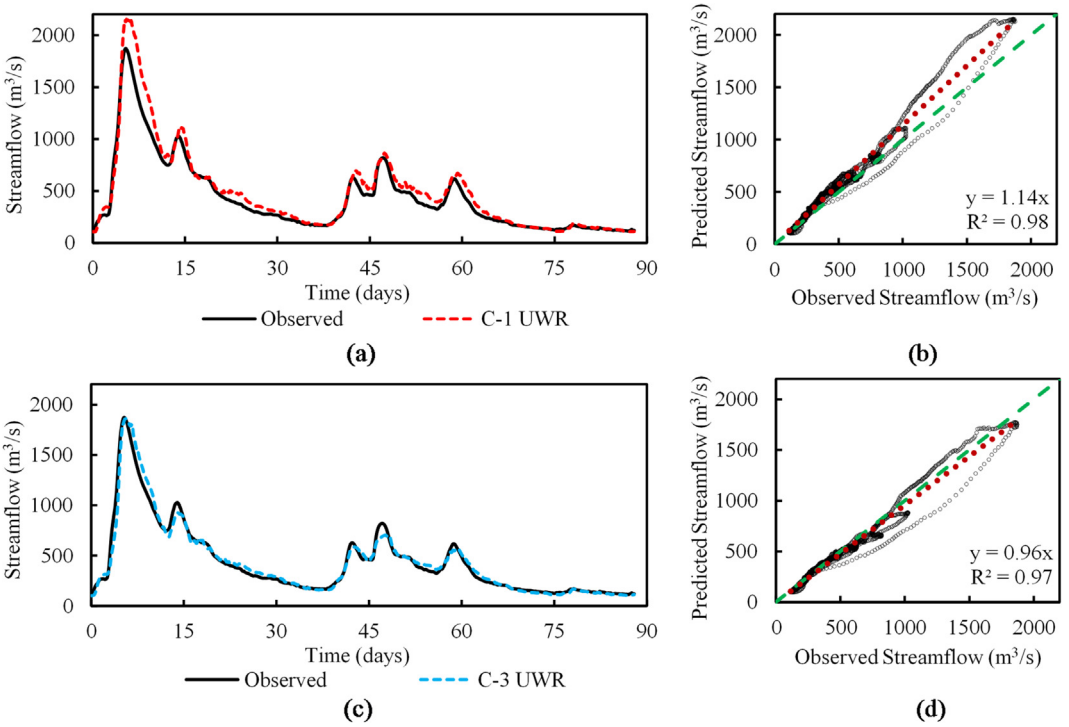

Fig. 10. Model comparison and validation for a three-month continuous simulation (February 17th to May 15th, 2018) for the UWR basin.

Table 7
Statistical analysis of streamflow prediction for model validation.

Model	R^2	NSE	Slope	PBIAS	RSR	Error Peak Flow (%)
C1-UWR	0.98	0.92	1.14	+12.1	0.28	+14.9
C3-UWR	0.97	0.97	0.96	−4.2	0.17	−5.3
C1-CR Putnam	0.74	0.50	1.26	+64.8	0.70	+41.6
C3-CR Putnam	0.95	0.95	0.99	−6.1	0.23	+12.1
C1-CR Brewster	0.68	0.18	1.38	+86.3	0.91	+23.4
C3-CR Brewster	0.85	0.85	0.95	+4.2	0.39	−21.1

continuous simulations.

To warrant a broader applicability of the integrated modeling approach, the C1 and C3 configurations are also tested for another watershed with significantly different physical characteristics from the UWR basin. Therefore, the East Branch Croton River (CR) basin with a drainage area of 210 km^2, situated in the state of New York, USA, is chosen as an additional validation site. As shown in Fig. 11, the land use for the CR basin is characterized by 56% forest cover, 23% developed, 11% agriculture, and 10% water. On the other hand, the land use for the UWR basin comprises of 7% forest, 9% developed, 82% agriculture, and 2% water (Table 1), highlighting the difference in the physical characteristics between the two watersheds. Additionally, unlike the Wabash River, which is channel flow dominated, the Croton River is a rainfall-runoff dominated stream surrounded by wetlands. The outlet of the CR basin is located at the USGS gage 01374505, East Branch Croton River at Brewster, NY as shown in Fig. 11. To aid a more extensive validation, the performance of C1 and C3 is also compared against observed data inside the watershed at an additional USGS gage 0137449480, East Branch Croton River near Putnam Lake, NY. Using the same modeling approach as the UWR basin, two models for the CR basin (referred as C1-CR and C3-CR) are simulated for a continuous

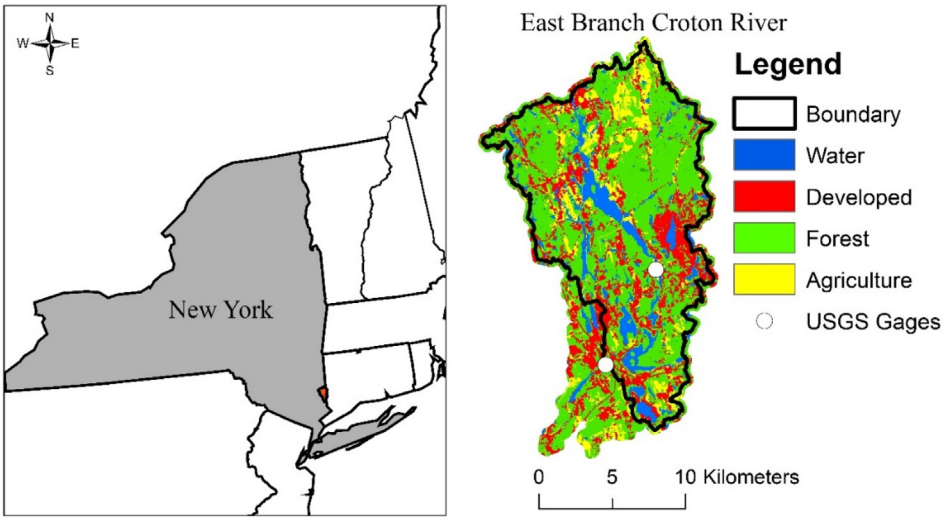

Fig. 11. Location map for East Branch Croton River Basin in New York.

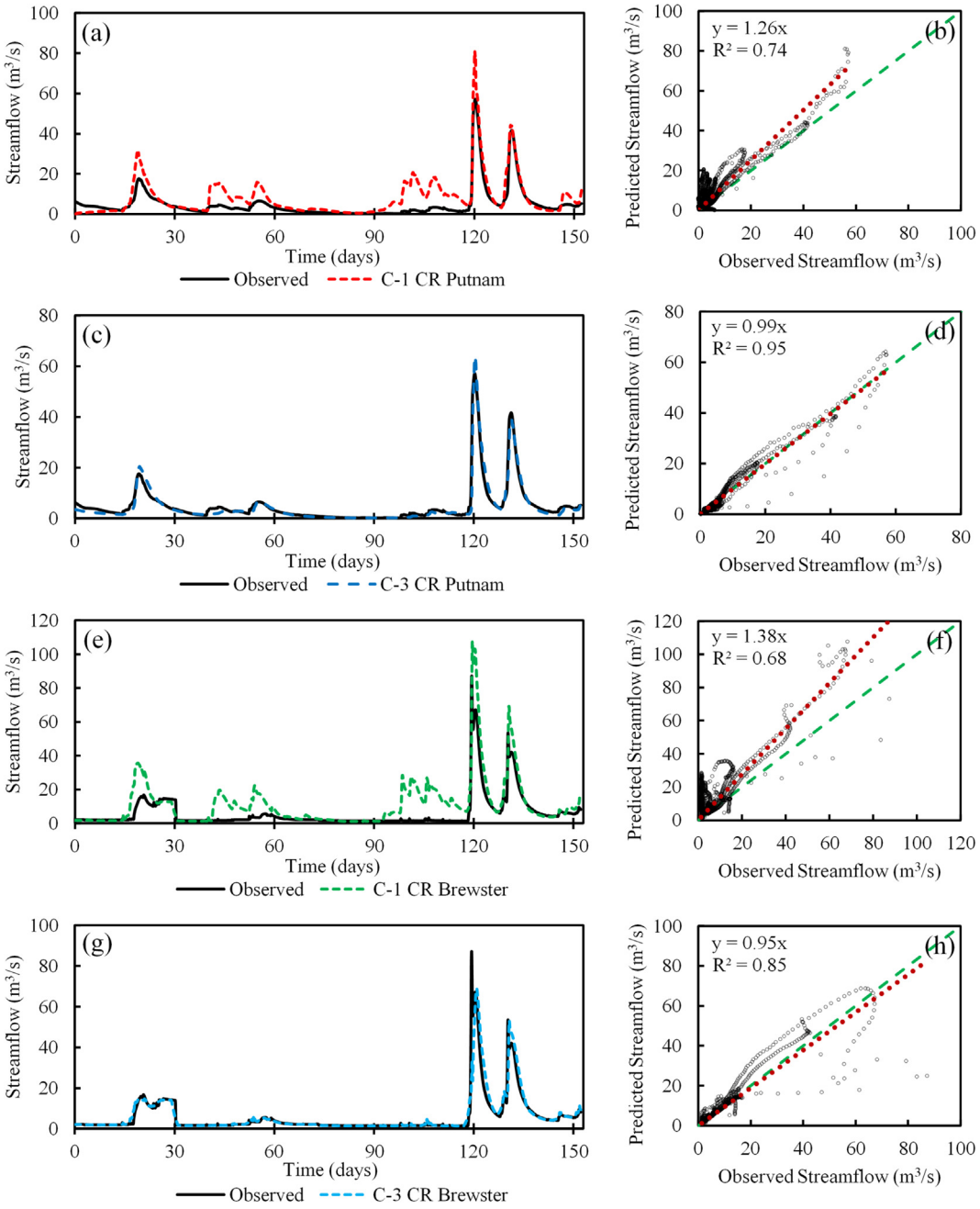

Fig. 12. Streamflow comparison against observed data across two gages for East Branch Croton River, NY for a five-month simulation (May 1st to September 30th, 2011).

seven-month period from March 1st to September 30th, 2011. To provide a longer time for incorporating antecedent conditions in the integrated model, the first two months are used as warm-up period, and the results are compared with the observed data from May 1st to September 30th, 2011.

The results (Fig. 12) highlight the inability of C1-CR to capture streamflow variability in small rainfall-runoff dominated catchments, especially for low flows. As shown in Fig. 12c and Table 7, C1-CR overpredicts both the high and low flows at Brewster (NSE = 0.18, PBIAS = +86.3%, and Error Peak Flow = +23.4%). It is evident from Fig. 12d that C3-CR (NSE = 0.85, PBIAS = +4.2%, and Error Peak Flow = −21.1%) has a superior performance compared to C1-CR. The difference in the performance between the two configurations becomes wider during long-term continuous simulations, especially for small rainfall events. A possible explanation for this difference is the shallow channel conveyance and existence of wetlands around the Croton River, which can cause higher river-floodplain interactions even during low flows, resulting in streamflow attenuation during small events, which is evident from Fig. 12b and d. When considering only the high flows which are more relevant to flood modeling, the performance of C1-CR is comparable to C3-CR at Brewster.

The difference in performance is also observed at Putnam (inside the watershed), where C1-CR (NSE = 0.50, PBIAS = +64.8%, and Error Peak Flow = +41.6%) overpredicts the streamflow (Fig. 12a) during the continuous simulation, and C3-CR (NSE = 0.95, PBIAS = −6.1%, and Error Peak Flow = +12.1%) captures the hydrograph variability including the peak flows more accurately (Fig. 12b). The results from Fig. 12 and Table 7 highlight the broader applicability of the integrated modeling approach (C3) for watershed with distinct physical characteristics.

As highlighted in Section 5.3, incorporating accurate antecedent conditions is highly essential in improving the predictive capacity of integrated models. This is also evident from the accurate performance of C3-CR, for which a sufficiently long warm-up period is chosen (2 months) to incorporate antecedent conditions more accurately. Therefore, during event-scale flood modeling, the rainfall distribution and streamflow patterns prior to the event should be carefully analyzed and saturated, dry or moderate soil moisture distribution should be used for characterizing initial conditions depending on the hydrologic time series preceding the flood events being simulated. While the performance of C3 is superior to C1 in both watersheds, this does not necessarily mean that the integrated models will obviously outperform the overland flow flood models across all watersheds. Since the physical processes involved in hydraulic and hydrologic modeling are scale dependent, the application of integrated modeling may not achieve significant improvements compared to using simpler surface-water transport models at small spatial scales for channel flow dominated streams, when the influence of rainfall and subsurface processes is diminished.

6. Summary and conclusions

Generally, hydrologic models are calibrated for streamflow while hydraulic models are calibrated for stage and extent of inundation. However, these three variables, streamflow, stage and extent of inundation are linked together, and are a function of multiple variables including topography, rainfall, soil type, land use, subsurface storage and evapotranspiration. This study highlights the discrepancies in simulating the river hydrodynamics when some of the underlying processes are not incorporated in the model. Specifically, the results from this study highlight the advantages of using integrated SW-GW models in simulating flood hydrodynamics. The following conclusions are drawn from this study:

1. A comparison of the model configurations shows that C1 produces the highest outflow volume since the change in storage is only dependent on topographic gradients and surface roughness, while C2 produces the smallest outflow volume since the water percolating below the vadose zone is lost from the water balance. The existence of dynamic WT in C3 reduces the water lost from the system, and therefore, the outflow volume is higher than C2. Overall, C3 produces the highest NSE and lowest PBIAS in estimating streamflow and stage compared to observed data.
2. Looking at only the impact of streamflow in affecting the extent of inundation, the results from this study hint at an underprediction of the extent of inundation by using the conventional surface water modeling approach (C1 or C2) compared to C3. However, in the absence of observed extent of inundation, this conclusion needs further evaluation.
3. Most hydraulic models are calibrated by modifying the roughness coefficients but the results from this study show that an incorporation of the SW-GW dynamics within the river system (C3) can improve the performance of models in estimating streamflow and stage without any extensive calibration. This reinforces the notion that the dynamic river stage should be simulated by including SW-GW interactions in the model instead of only calibrating the roughness coefficient.
4. The existing WT location and antecedent soil moisture conditions can have a significant impact on the streamflow, stage and flood inundation area. The results suggest that saturated subsurface conditions (W) can severely increase the inundation area. On the other hand, dry subsurface conditions (D) can reduce the overall impact of flood events. Incorporating accurate antecedent conditions is essential for predicting flood responses accurately, and therefore, adequate warm-up period should be chosen for integrated models depending on the spatial scale of the watershed and temporal scale of simulations.
5. The validation of C3 for an independent continuous 3-month simulation for the UWR basin, and for a 5-month simulation for the CR basin with different physical characteristics highlights the broad applicability of the integrated modeling approach.

Although the results from this study are promising, and the modeling approach proposed here is relatively more comprehensive, some of the modeling components can be further improved to enhance the findings. For example, this study incorporates soil redistribution in the vadose zone using vertically homogeneous soil zones, where the soil moisture and subsequent GW recharge is computed using a non-iterative kinematic approach, and hence, the integrated models do not incorporate lateral flows in the vadose zone. This assumption works well for large flood events with a high intensity of rainfall, as the soil moisture profile closely resembles a sharp wetting front (cylinder). However, infiltration does not occur cylindrically, instead, percolates through the soil system in three dimensions. Lateral flows can not only influence the volume and location of GW recharge, but also the magnitude of streamflow, although the residence time may be large (Hughes, 2010). This study assumes that the vertical percolation dominates during the simulation period, which may not be true during low flow conditions or in other watersheds.

For a more realistic estimation of the soil moisture redistribution during continuous simulations, numerical solution of the 3D Richards' equation using finite element formulations can be used. However, obtaining adequate data to parameterize a 3D model of unsaturated low is very difficult. Additionally, when dealing with large watersheds, representing the vadose zone using the 3D form of Richard's equation becomes computationally expensive and impractical for the purpose of flood modeling. In this regard, models such as ParFlow and HydroGeoSphere, which offer a fully integrated 3D solution of unsaturated and saturated subsurface flow aided by high performance computing can be incorporated in future studies (Brunner and Simmons, 2012; Kollet and Maxwell, 2006). Finally, the effect of preferential flows is also neglected in this study. Preferential flow through macropores can bypass the entire unsaturated soil column and accelerate the transport of water into the streams (Alaoui et al., 2011). Therefore, preferential flow through the soil matrix should be incorporated in regions where the soil properties are conducive for its existence, although obtaining accurate data to characterize the preferential flow paths is very challenging.

It should be noted that the antecedent (initial) soil conditions are chosen at field capacity for all simulations of the integrated (C3) model. This is done as the exact soil moisture distribution is unknown at the beginning of the simulation. Similarly, the initial WT surface used in C3 is generated by simulating steady-state conditions for one month and assuming that the WT surface is in equilibrium. Further, this study uses contour maps for calculating the initial WT depths, but these maps are sparsely distributed and are not available for majority of the watersheds in the world. Therefore, it is possible that the superior performance of the C3 model is influenced by the choice of antecedent soil moisture distribution and the availability of accurate WT information for the UWR basin in Indiana. In the absence of such information, it is necessary to incorporate a substantially long warm-up period (e.g. two months for CR basin), which can help in balancing the soil moisture profile before the actual event is simulated. However, this warm-up period should be chosen depending on the scale of the watershed, magnitude of the event, and climatic conditions preceding the event for accurately incorporating the antecedent conditions (Berthet et al., 2009; Pathiraja et al., 2012; Zehe and Blöschl, 2004).

Similarly, the initial WT location for integrated modeling can be simulated by assuming that the WT is located at a fixed depth below the ground surface (e.g. 2 m for the CR basin), followed by a rebalancing of the WT hydraulic heads using a long steady-state simulation. This method is used to initialize the WT for the C3-CR model and the results presented here support its applicability. Another alternative to this

approach is to start the model simulation during a dry season by assuming completely saturated subsurface conditions (WT = ground surface) and simulating the model for a period of more than three months to let the model obtain equilibrium before the onset of the rainy (wet) season. Regardless, these methods need to be validated across several other watersheds with different physiological characteristics to justify a broader applicability.

Evapotranspiration is an important physical process that can impact river hydrodynamics and other hydrologic variables in the water cycle, especially during continuous simulations of several months. One of the limitations of this study is that ET is only incorporated in the 7-month simulation of the CR basin (Section 5.4). As shown in the results, the absence of ET does not affect the performance of C3 in estimating streamflow and stage for the UWR basin. This could be due to the large spatiotemporal scale of rainfall distribution, high relative humidity and cloud cover over many days in the simulation period. While the impact of ET may be less significant for the events in this study, the absence of ET may result in erroneous estimation of streamflow and stage during other events, and at other locations. Therefore, the effect of ET should be incorporated in future studies for long-term-continuous integrated modeling.

Another limitation of this study is the absence of stormwater drainage system in the models, especially for Croton River basin with a 23% developed area. The water discharging into the open channels from the storm drains can influence the magnitude of peak streamflow, time-of-peak, and duration of inundation in urban areas. However, studies on distributed modeling of urban areas have shown that the impact of stormwater drainage in affecting streamflow is diminished during extreme events as the conveyance in the open channels is significantly higher than stormwater drains (Ogden et al., 2011). Regardless, storm drains can increase flood peaks in the river channels during small to moderate rainfall events, and therefore, should be included in future studies especially during continuous simulations containing multiple rainfall events. While the effect of urban stormwater system is not included in this study, the effect of imperviousness in developed regions resulting in reduced infiltration is incorporated in the watersheds used in this study.

While it may be argued that the integrated model performance is specific to the watersheds used for the analysis, the broader goal here is to highlight the reduction in modeling uncertainties when SW-GW interactions are incorporated in modeling and mapping the flood inundation. Watersheds with different physical characteristics react to rainfall events of similar magnitude and intensities differently. Similarly, the groundwater characteristics of the region control the amount of seepage, recharge, and WT fluctuations. Therefore, the integration of subsurface processes may achieve improvements of different degrees for watersheds depending on the physiographic and hydrogeologic characteristics. However, even a watershed with a completely different land use classification, aquifer characterization, and soil classification, can be modeled accurately, when the physical processes driving the hydrologic variability are incorporated. For example, a watershed with an urban land use, low infiltration capacity, and clayey aquifer will undergo diminished SW-GW interactions. While the GW recharge and vadose zone storage might reduce in such a scenario, excess rainfall contributions due to increased impervious cover and reduced infiltration will become more significant, and the inability of traditional streamflow driven flood models to account for excess rainfall in the watershed, may still result in poor performance. Alternatively, if excess rainfall and infiltration calculations are integrated with channel flow for such watersheds, it might yield a more realistic representation of the river-floodplain hydrodynamics, and therefore, the overall flood prediction would be more reliable. Therefore, future studies should incorporate the effect of antecedent atmospheric and subsurface conditions in flood models for more reliable flood determination.

Declaration of Competing Interest

None.

Acknowledgements

Data used in this paper is listed throughout the manuscript and can also be made available upon request from the authors. This work was supported by grants from the Indiana Water Resources Research Center. We thank Dr. Marty Frisbee from Purdue University for his help in obtaining the groundwater data for Indiana. The authors also thank Kimberly Peterson from the Lyles School of Civil Engineering for proofreading the paper. We also thank the editor, Dr. Emmanouil Anagnostou, the associate editor, Dr. Dingbao Wang, the reviewer, Dr. Edwin H. Sutanudjaja and the one anonymous reviewer for providing a thoughtful and constructive feedback.

Appendix A

This section provides supplementary information on the overland flow processes including the relevant equations and numerical formulations that are used in this study. Although ICPR includes both one-dimensional (1D) and two-dimensional (2D) surface flow, 1D flow is not used in this study. Regardless, the basic computational framework for both 1D and 2D surface is based on the node-link concept using a finite volume approach that allows for a single fully-integrated system of equations to be developed and solved simultaneously. Therefore, the 1D and 2D surface hydraulics do not have to be coupled. Nodes are specific locations in the modeling domain where WSE are calculated. Links are used to connect and move water from one node to another. The surface flows are calculated along the links based on the WSE values at the connecting nodes. Some of the examples of 1D links include, pipes, weirs, channel segments, bridges and pump stations. The rainfall-runoff occurs for basins or catchment areas and runoff from the basins is delivered to the surface nodes. Although not used in this study, the traditional hydrologic methods such as the NRCS unit hydrograph method can also be used in ICPR.

A flexible triangular computational mesh is used for 2D overflow and is generated automatically based on the various graphical features developed by the modeler. The vertices of the triangles are treated as nodes and the sides of the triangles become overland flow links. The control volumes are formed around the vertices and extend to the midpoints of the triangle sides and to the geometric center of the triangle as shown in Fig. A.1(a). The control volumes become the catchment areas for the rainfall-runoff processes. The collection of control volumes is referred to as the “honeycomb” mesh which is intersection with soils and land use maps forming a system of sub-polygons (see Fig. A.1(b)). Rainfall is applied to each sub-polygon and any water that is does not percolate into the soil is aggregated by the respective control volume and delivered to the corresponding 2D surface node.

A diamond mesh as depicted in Fig. A.1(c) is simultaneously formed along the triangle edges (i.e. 2D overland flow links) and is used to develop the edge properties. The diamond mesh is intersected with a roughness zone map layer to determine the average roughness characteristics for each triangle edge. Each triangle edge is idealized into an equivalent rectangle for maximizing the computational efficiency. Edge properties are calculated using Eqs. (A.1)–(A.3) and Fig. A.1(c).

$$L = (2/3)L_{A-B} \tag{A.1}$$

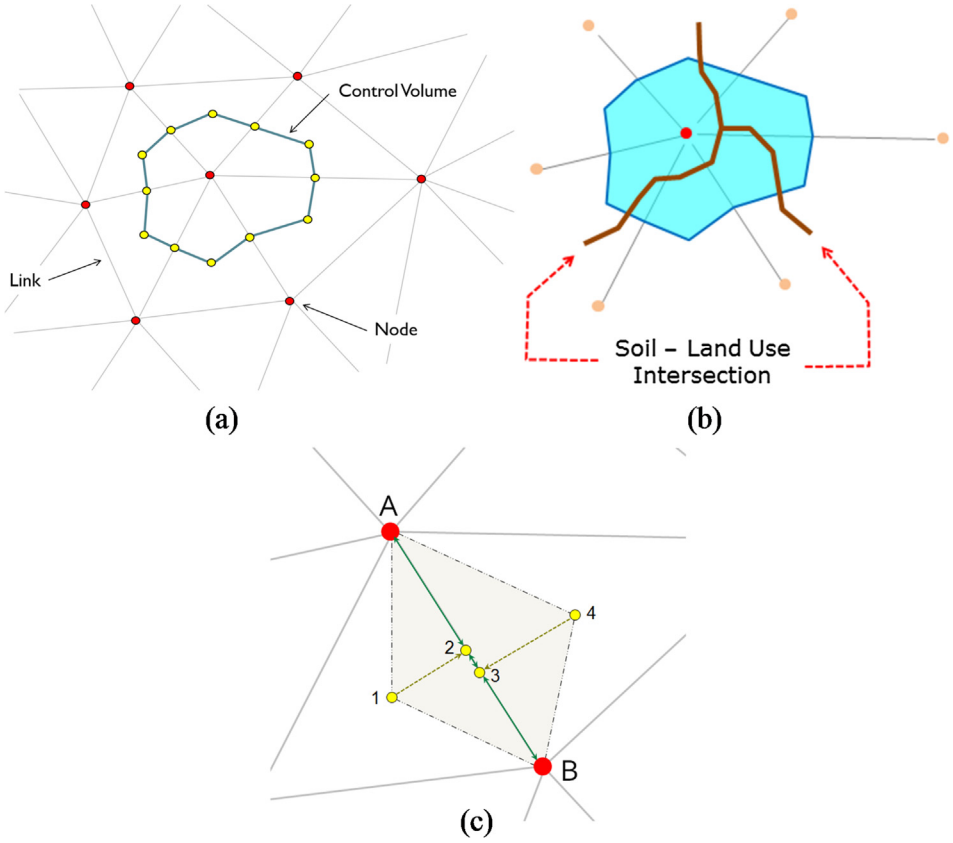

Fig. A1. (a) Link, node and control volume development in a flexible triangular mesh; (b) Control volume intersection with soils and land use map layers; and (c) Overland flow link (triangle edge) development.

$$W = A_{diamond}/L \tag{A.2}$$

$$S_{2D} = [S_{A-B}^2 + (S_{1-2} + S_{3-4})^2]^{1/2} \tag{A.3}$$

where, L = equivalent rectangular length; L_{A-B} = the length from vertex A to vertex B; W = equivalent width; $A_{diamond}$ = the area of the diamond along a triangle edge; S_{2D} = average two-dimensional ground slope along a triangular edge; S_{A-B} = the longitudinal ground slope between vertex A and vertex B; S_{1-2} = the ground cross-slope between the points 1 and 2; and S_{3-4} = the ground cross-slope between points 3 and 4.

The mass balance equations used in ICPR for every time-step are presented in Eqs. (A.4)–(A.7). These equations are applied at each node and at every time-step to evaluate the volume of water from individual processes such as seepage, direct runoff (rainfall excess) and link flow generation. These equations apply to both 1D and 2D surface hydraulics.

$$dz = \left(\frac{(Q_{in} - Q_{out})}{A_{surface}}\right)dt \tag{A.4}$$

$$Z_{t+dt} = Z_t + dz \tag{A.5}$$

$$Q_{in} = \sum Q_{link_{in}} + \sum Q_{excess} + \sum Q_{external} + \sum Q_{seepage} \tag{A.6}$$

$$Q_{out} = \sum Q_{link_{out}} + \sum Q_{irrigation} \tag{A.7}$$

where, dz = incremental change in stage; dt = computational time-step; Q_{in} = total inflow rate; Q_{out} = total outflow rate; $A_{surface}$ = wet surface area; Z_{t+dt} = new WSE; Z_t = WSE at previous time-step; $\sum Q_{link_{in}}$ = sum of all link flow rates entering a control volume; $\sum Q_{link_{out}}$ = sum of all link flow rates leaving the control volume; $\sum Q_{excess}$ = sum of rainfall excess rates for polygons in control volume; $\sum Q_{external}$ = sum of all inflows from external sources such as streamflow gages; $\sum Q_{seepage}$ = sum of lateral seepage inflow from groundwater model; $\sum Q_{irrigation}$ = sum of water pulled out of the system for irrigation.

The ICPR model includes three solution options for 2D overland flow: (1) the one-dimensional St. Venant equation; (2) the energy equation; and (3) the diffusive wave equation. The diffusive wave equation is used in this study for maintaining computational efficiency. Details of the St. Venant and energy formulations can be found in Streamline Technologies, 2018. The diffusive wave formulations for 2D overland flow are presented in Eqs. (A.8)–(A.10).

$$Q = \left(\frac{Z_1 - Z_2}{\Delta x C_f}\right)^{\frac{1}{2}} \tag{A.8}$$

$$C_f = \left(\frac{1}{K}\right)^2 \tag{A.9}$$

$$K = \frac{CR^{\frac{2}{3}}A}{n} \tag{A.10}$$

where, Q = overland flow rate; A = cross-sectional area; t = time; g = acceleration due to gravity; Z_1 = upstream WSE; Z_2 = downstream WSE; Δx = distance in direction of flow; n = Manning's roughness coefficient; R = hydraulic radius; C_f = conveyance factor; Δx = distance between adjacent cross-sections.

ICPR uses an exponential decay function (shown in Eqs. (A.11) and (A.12)) dependent on surface depth to incorporate the variability in surface roughness (Arcement and Schneider, 1984).

$$n = n_{shallow}e^{(k)(d)} \tag{A.11}$$

$$k = \frac{ln\left(\frac{n_{deep}}{n_{shallow}}\right)}{d_{max}} \tag{A.12}$$

where, n = Manning's roughness at depth d; $n_{shallow}$ = Manning's roughness at ground surface; n_{deep} = Manning's roughness at depth $\geq d_{max}$; k = exponential decay factor; d = depth of flow; d_{max} = user specified maximum depth (0.91 m or 3 feet in this study) for transitioning to n_{deep}.

A vertical soil layer approach (referred to as the refined Green-Ampt method) is used in this study to model unsaturated flow in the vadose zone for each sub-polygon in the control volumes formed around the triangle vertices. Although homogeneous soil zones are used, the soil column is discretized into multiple computational cells and soil moisture is tracked for each cell as described in the main body of this document. Fluxes across cells are based on the unsaturated vertical conductivity. The Brooks-Corey soil water retention–hydraulic conductivity relationship (Rawls and Brakensiek, 1982), shown in Eq. (A.13), is used to determine unsaturated conductivities based on initial soil moisture contents.

$$\frac{K(\theta)}{K_s} = \left(\frac{\theta - \theta_r}{\varphi - \theta_r}\right)^n \tag{A.13}$$

where, θ = current moisture content; θ_r = residual moisture content; φ = saturated moisture content; $K(\theta)$ = unsaturated vertical conductivity at θ; K_s = saturated vertical conductivity; $n = 3 + \frac{2}{\lambda}$; and λ = pore size index.

The reference evapotranspiration rates are evaluated using the Penman-Monteith Equation (shown in Eq. (A.14)) as described in Allen et al. (1998).

$$RET = \frac{0.408\Delta(R_n - G) + \gamma\frac{900}{T+273}u_2(e_s - e_a)}{\Delta + \gamma(1 + 0.34u_2)} \tag{A.14}$$

where, RET = reference evapotranspiration (mm day^{-1}); R_n = net radiation at crop surface (MJ m^{-2} day^{-1}); G = soil heat flux density (MJ m^{-2} day^{-1}); T = air temperature at 2 m height (°C); u_2 = wind speed at 2 m height (m s^{-1}); e_s = saturation vapor pressure (kPa); e_a = actual vapor pressure (kPa); Δ = slope vapor pressure curve (kPA °C^{-1}); and γ = psychrometric constant (kPA °C^{-1}). To evaluate the coefficients in A.16 and subsequently, RET, the empirical equations provided in Allen et al. (1998), are used in conjunction with meteorological data. The meteorological data for calculating RET in ICPR includes observations of daily maximum and minimum temperature, dew point temperature, cloud cover percentage, wind speed and altitude.

Appendix B

Detailed Description of the 2D GW Flow Finite Element Formulation used in ICPR (modified from Martínez, 1989; Streamline Technologies, 2018).

The continuity equation for unsteady phreatic 2D GW flow is given below:

$$n\frac{\partial h}{\partial t} = -\frac{\partial(uh)}{\partial x} - \frac{\partial(vh)}{\partial y} \tag{B.1}$$

where, n is the fillable porosity (or specific yield); h is the GW elevation (piezometric head); u, v are the velocity vector components; t is time; *and* x, y are the Cartesian coordinates. Additionally, the velocity vectors for an isotropic porous media are expressed using the following equation:

$$u = -K.\frac{\partial h}{\partial x};\ \text{and},\ v = -K.\frac{\partial h}{\partial y} \tag{B.2}$$

where, K is the permeability (conductivity) of the porous media. On substituting Eq. (B.2) in B.1, and adding an external flow f, representing the total flow coming into GW region in the form of seepage and recharge, the following equation is obtained:

$$f + n\frac{\partial h}{\partial t} = \frac{\partial(Kh.\ h_x)}{\partial x} + \frac{\partial(Kh.h_y)}{\partial y} \tag{B.3}$$

Here, h_x and h_y are partial derivative notations. Since the GW region is divided into a triangular mesh network, the total aquifer area is the sum of partial areas of the all the triangles in the mesh network. Eq. (B.3) is then expressed as a summation function of each individual triangle using a Galerkin approximation, and the resultant equation is shown below:

$$\iint_R N_i.\ I.\ dxdy = \sum_{j=1}^{N_e}\iint_{e_j} N_i.\ I.\ dxdy = \{0\} \tag{B.4}$$

where, $I = \frac{\partial(Kh.h_x)}{\partial x} + \frac{\partial(Kh.h_y)}{\partial y} - \left(f + n\frac{\partial h}{\partial t}\right)$; $N_i = \varnothing_i(x, y)$, the dimensionless shape function for any node i of the triangle; e_j is any triangular element j;

N_e is the total number of elements in the aquifer region; R is the total aquifer region; {0} is the null vector with the number of components equal to the total number of nodes. On applying integration by parts and Green's Theorem over the integration of an individual element e_j, the following equation is obtained:

$$\iint_{e_j} N_i.\ I.\ dxdy = \iint_{e_j} I_1.\ dxdy + \iint_{e_j} I_2.\ dxdy - \int_{C_{e_j}} I_3.\ dL = 0 \tag{B.5}$$

where, $I_1 = Kh\left\{\frac{\partial N_i}{\partial x}.\ h_x + \frac{\partial h}{\partial y}.\ h_y\right\}$; $I_2 = N_i\left(f + n\frac{\partial h}{\partial t}\right)$; $I_3 = N_i(Kh).\ h_s$; h_x, h_y, and h_s are notations for partial derivatives; s is the flow direction; C_{e_j} is the boundary of the element e_j; dL is the differential length along the boundary such that $h_s dL = h_x dy - h_y dx$. Within ICPR, Eq. (B.5) is expressed and solved for six nodes, which are formed using three triangle vertices and three mid-side points, and the solution is approximated using finite element formulations for each individual triangle over the entire mesh network. Overall, the variation of head (h) for each triangle is expressed using the following equation:

$$h = Ax^2 + By^2 + Cxy + Dx + Ey + F \tag{B.6}$$

The shape function N_i is defined for each one the six nodes using six equations so that the overall head (h) anywhere inside the triangle is a linear combination of the head (h) at the six nodes, which gives:

$$h = \sum_{k=1}^{6} N_k h_k \tag{B.7}$$

Using a cyclic permutation involving calculation of six shape functions that are compatible with Eqs. (B.7) and calculating the head (h) derivatives from Eq. (B.6), the three integrals in Eq. (B.5) are evaluated at each time-step for the entire mesh network. Finally, the seepage rates along a sloping ground surface, river bank or seepage faces on a hill are calculated using Eq. (B.8):

$$Q_{seepage} = \frac{(h_1 - h_2) \times (A) \times \varphi_b}{dt_{gw}} \tag{B.8}$$

where, $Q_{seepage}$ = seepage rate (L^3T^{-1}); h_1 = calculated WT elevation (L); h_2 = ground surface elevation at node (L); A = groundwater control volume surface area (L^2); φ_b = below ground fillable porosity; and dt_{gw} = groundwater computational time increment (T).

References

Ahmad, H., Miller, J.W., George, R.D., 2014. Minimizing pond size using an off-site pond in a closed basin: a storm flow mitigation design and evaluation. Int. J. Sustain. Dev. Plan. 9, 211–224. https://doi.org/10.2495/SDP-V9-N2-211-224.

Alaoui, A., Caduff, U., Gerke, H.H., Weingartner, R., 2011. Preferential flow effects on infiltration and runoff in grassland and forest soils. Vadose Zone J. 10, 367. https://doi.org/10.2136/vzj2010.0076.

Allen, R.G., Luis, S.P., Raes, D., Smith, M., 1998. Crop Evapotranspiration: Guidelines for Computing Crop Water Requirements. FAO Irrig. Drain. Pap. No. 56., Food Agric. Organ. L. Water, Rome, Italy10.1016/j.eja.2010.12.001.

Arcement Jr., G.J., Schneider, V.R., 1984. Guide for Selecting Manning's Roughness Coefficients for Natural Channels. Fed. Highw. Adm. FHWA-TS- 84, pp. 68.

Arnold, J.G., Moriasi, D.N., Gassman, P.W., Abbaspour, K.C., White, M.J., Srinivasan, R., Santhi, C., Harmel, R.D., Van Griensven, A., VanLiew, M.W., Kannan, N., Jha, M.K., 2012. Swat: Model Use, Calibration, and Validation. Trans. ASABE 55 1491–1508.

Bales, J.D., Wagner, C.R., 2009. Sources of uncertainty in flood inundation maps. J. Flood Risk Manage. 2, 139–147. https://doi.org/10.1111/j.1753-318X.2009.01029.x.

Bates, P., De Roo, A., 2000. A simple raster-based model for flood inundation simulation. J. Hydrol. 236, 54–77. https://doi.org/10.1016/S0022-1694(00)00278-X.

Begnudelli, L., Sanders, B.F., 2006. Unstructured grid finite volume algorithm for shallow-water flow and transport with wetting and drying. J. Hydraul. Eng. 132, 371–384.

Berthet, L., Andréassian, V., Perrin, C., Javelle, P., 2009. How crucial is it to account for the antecedent moisture conditions in flood forecasting? Comparison of event-based and continuous approaches on 178 catchments. Hydrol. Earth Syst. Sci. 13, 819–831. https://doi.org/10.5194/hess-13-819-2009.

Beven, K., 1993. Prophecy, reality and uncertainty in distributed hydrological modelling. Adv. Water Resour. 16, 41–51. https://doi.org/10.1016/0309-1708(93)90028-E.

Bhuyian, N.M., Kalyanapu, A.J., Nardi, F., 2015. Approach to digital elevation model correction by improving channel conveyance. J. Hydrol. Eng. ASCE 2015 (20), 1–10. https://doi.org/10.1061/(ASCE)HE.1943-5584.0001020.

Bixio, A.C., Gambolati, G., Paniconi, C., Putti, M., Shestopalov, V.M., Bublias, V.N., Bohuslavsky, A.S., Kasteltseva, N.B., Rudenko, Y.F., 2002. Modeling groundwater-surface water interactions including effects of morphogenetic depressions in the Chernobyl exclusion zone. Environ. Geol. 42, 162–177. https://doi.org/10.1007/s00254-001-0486-7.

Bloschl, G., Sivapalan, M., 1995. Scale issues in hydrological modelling: a review. Hydrol. Process. 9, 251–290.

Booker, A.S., 2006. Modeling the 100-Year Flood Using GIS. Master's Thesis. A Flood Analysis in the Avon Park Watershed. University of South Florida.

Brunner, G., 2010. HEC-RAS, River Analysis System Hydraulic Reference Manual.

Brunner, P., Simmons, C.T., 2012. HydroGeoSphere: a fully integrated, physically based hydrological model. Ground Water 50, 170–176. https://doi.org/10.1111/j.1745-6584.2011.00882.x.

Bunya, S., Dietrich, J.C., Westerink, J.J., Ebersole, B.A., Smith, J.M., Atkinson, J.H., Jensen, R., Resio, D.T., Luettich, R.A., Dawson, C., Cardone, V.J., Cox, A.T., Powell, M.D., Westerink, H.J., Roberts, H.J., 2010. A high-resolution coupled riverine flow, tide, wind, wind wave, and storm surge model for southern louisiana and mississippi. Part I: model development and validation. Mon. Weather Rev. 138, 345–377. https://doi.org/10.1175/2009MWR2907.1.

Te Chow, V., 1959. Open Channel Hydraulics. McGraw-Hill B. Company, Inc. 10.1016/B978-0-7506-6857-6.X5000-0.

Cohen, S., Brakenridge, G.R., Kettner, A., Bates, B., Nelson, J., McDonald, R., Huang, Y.-F., Munasinghe, D., Zhang, J., 2018. Estimating floodwater depths from flood inundation maps and topography. JAWRA J. Am. Water Resour. Assoc. 54, 847–858. https://doi.org/10.1111/1752-1688.12609.

Cook, A., Merwade, V., 2009. Effect of topographic data, geometric configuration and modeling approach on flood inundation mapping. J. Hydrol. 377, 131–142. https://doi.org/10.1016/j.jhydrol.2009.08.015.

Cooper, H.H.J., Rorabaugh, M.I., 1963. Ground-water movements and bank storage due to flood stages in surface streams. U. S. Geol. Surv. Water-Supply Pap. 343–366 https://doi.org/Water-Supply Paper 1536-J.

David, C.H., Habets, F., Maidment, D.R., Yang, Z.L., 2011a. RAPID applied to the SIM-France model. Hydrol. Processes 25, 3412–3425. https://doi.org/10.1002/hyp.8070.

David, C.H., Maidment, D.R., Niu, G.-Y., Yang, Z.-L., Habets, F., Eijkhout, V., 2011b. River network routing on the NHDPlus dataset. J. Hydrometeorol. 12, 913–934. https://doi.org/10.1175/2011JHM1345.1.

Dey, S., Saksena, S., Merwade, V., 2019. Assessing the effect of different bathymetric models on hydraulic simulation of rivers in data sparse regions. J. Hydrol. 575, 838–851. https://doi.org/10.1016/j.jhydrol.2019.05.085.

Di Baldassarre, G., Schumann, G., Bates, P.D., 2009. A technique for the calibration of hydraulic models using uncertain satellite observations of flood extent. J. Hydrol. 367, 276–282. https://doi.org/10.1016/j.jhydrol.2009.01.020.

Dimitriadis, P., Tegos, A., Oikonomou, A., Pagana, V., Koukouvinos, A., Mamassis, N., Koutsoyiannis, D., Efstratiadis, A., 2016. Comparative evaluation of 1D and quasi-2D hydraulic models based on benchmark and real-world applications for uncertainty assessment in flood mapping. J. Hydrol. 534, 478–492. https://doi.org/10.1016/j.jhydrol.2016.01.020.

Domingues, M.O., Gomes, S.M., Roussel, O., Schneider, K., 2008. An adaptive multiresolution scheme with local time stepping for evolutionary PDEs. J. Comput. Phys. 227, 3758–3780. https://doi.org/10.1016/j.jcp.2007.11.046.

Downer, C.W., Ogden, F.L., 2006. Gridded Surface Subsurface Hydrologic Analysis (GSSHA) User's Manual, Version 1.43 for Watershed Modeling System 6.1. US Army Corps Eng. Eng. Res. Dev. Cent.

Downer, C.W., Ogden, F.L., Martin, W.D., Harmon, R.S., 2002. Theory, development, and applicability of the surface water hydrologic model CASC2D. Hydrol. Processes 16, 255–275. https://doi.org/10.1002/hyp.338.

Faulkner, B.R., Renée Brooks, J., Forshay, K.J., Cline, S.P., 2012. Hyporheic flow patterns in relation to large river floodplain attributes. J. Hydrol. 448–449, 161–173. https://doi.org/10.1016/j.jhydrol.2012.04.039.

Fleckenstein, J.H., Krause, S., Hannah, D.M., Boano, F., 2010. Groundwater-surface water interactions: new methods and models to improve understanding of processes and dynamics. Adv. Water Resour. 33, 1291–1295. https://doi.org/10.1016/j.advwatres.2010.09.011.

Follum, M.L., Tavakoly, A.A., Niemann, J.D., Snow, A.D., 2016. AutoRAPID: a model for prompt streamflow estimation and flood inundation mapping over regional to continental extents. J. Am. Water Resour. Assoc. 80523, 1–20. https://doi.org/10.1111/1752-1688.12476.

Frisbee, M.D., Meyers, Z.P., Stewart-Maddox, N.S., Caffee, M.W., Bogeholz, P., Hughes, M.N., 2017. What is the source of baseflow in agriculturally fragmented catchments? Complex groundwater/surface-water interactions in three tributary catchments of the Wabash River, Indiana USA. Hydrol. Process. 31, 4019–4038. https://doi.org/10.1002/hyp.11345.

Gleeson, T., Manning, A.H., 2008. Regional groundwater flow in mountainous terrain: three-dimensional simulations of topographic and hydrogeologic controls. Water Resour. Res. 44. https://doi.org/10.1029/2008WR006848.

Grimaldi, S., Petroselli, A., Arcangeletti, E., Nardi, F., 2013. Flood mapping in ungauged basins using fully continuous hydrologic-hydraulic modeling. J. Hydrol. 487, 39–47. https://doi.org/10.1016/j.jhydrol.2013.02.023.

Gupta, H.V., Sorooshian, S., Yapo, O.P., 1999. Status of automatic calibration for hydrologic models: comparison with multilevel expert calibration. J. Hydrol. Eng. 4, 135–143. https://doi.org/10.1002/fut.20174.

Hall, J., Sayers, P., Dawson, R., 2005. National-scale assessment of current and future flood risk in England and Wales. Nat. Hazards 36, 147–164. https://doi.org/10.1007/s11069-004-4546-7.

Hughes, A.G., Vounaki, T., Peach, D.W., Ireson, A.M., Jackson, C.R., Butler, A.P., Bloomfield, J.P., Finch, J., Wheater, H.S., 2011. Flood risk from groundwater: examples from a Chalk catchment in southern England. J. Flood Risk Manage. 4, 143–155. https://doi.org/10.1111/j.1753-318X.2011.01095.x.

Hughes, D.A., 2010. Unsaturated zone fracture flow contributions to stream flow: evidence for the process in South Africa and its importance. Hydrol. Process. 24, 767–774. https://doi.org/10.1002/hyp.7521.

Hughes, J.D., Liu, J., 2008. MIKE SHE: software for integrated surface water/ground water modeling. Ground Water 46, 797–802. https://doi.org/10.1111/j.1745-6584.2008.00500.x.

Ivanov, V.Y., Vivoni, E.R., Bras, R.L., Entekhabi, D., 2004. Catchment hydrologic response with a fully distributed triangulated irregular network model. Water Resour. Res. 40, 1–23. https://doi.org/10.1029/2004WR003218.

Jackson, S.R., Maidment, D.R., 2014. RiverML: A Harmonized Transfer Language for River Hydraulic Models, CRWR Online Report 14–5. Cent. Res. Water Resour. Univ, Texas Austin.

Joyce, J., Bin Chang, N., Harji, R., Ruppert, T., Singhofen, P., 2017. Cascade impact of hurricane movement, storm tidal surge, sea level rise and precipitation variability on flood assessment in a coastal urban watershed. Clim. Dyn. 1–27. https://doi.org/10.1007/s00382-017-3930-4.

Kaser, D., Graf, T., Cochand, F., Mclaren, R., Therrien, R., Brunner, P., 2014. Channel representation in physically based models coupling groundwater and surface water: pitfalls and how to avoid them. Groundwater 52, 827–836. https://doi.org/10.1111/gwat.12143.

Kidmose, J., Troldborg, L., Refsgaard, J.C., Bischoff, N., 2015. Coupling of a distributed hydrological model with an urban storm water model for impact analysis of forced infiltration. J. Hydrol. 525, 506–520. https://doi.org/10.1016/j.jhydrol.2015.04.007.

Kollet, S.J., Maxwell, R.M., 2008. Capturing the influence of groundwater dynamics on land surface processes using an integrated, distributed watershed model. Water Resour. Res. 44. https://doi.org/10.1029/2007WR006004.

Kollet, S.J., Maxwell, R.M., 2006. Integrated surface-groundwater flow modeling: a free-surface overland flow boundary condition in a parallel groundwater flow model. Adv. Water Resour. 29, 945–958. https://doi.org/10.1016/j.advwatres.2005.08.006.

Kuiper, L.K., 1981. A comparison of the incomplete Cholesky-Conjugate Gradient Method with the strongly implicit method as applied to the solution of two-dimensional groundwater flow equations. Water Resour. Res. 17, 1082–1086. https://doi.org/10.1029/WR017i004p01082.

Legleiter, C.J., Kyriakidis, P.C., McDonald, R.R., Nelson, J.M., 2011. Effects of uncertain topographic input data on two-dimensional flow modeling in a gravel-bed river. Water Resour. Res. 47, 1–24. https://doi.org/10.1029/2010WR009618.

Van Liew, M.W., Arnold, J.G., Bosch, D.D., 2005. Problems and potential of auto-calibrating a hydrologic model. Trans. ASAE 48, 1025–1040.

Liu, G., Schwartz, F.W., Tseng, K.-H., Shum, C.K., 2015. Discharge and water-depth estimates for ungauged rivers: combining hydrologic, hydraulic, and inverse modeling with stage and water-area measurements from satellites. Water Resour. Res. 51, 6017–6035. https://doi.org/10.1002/2014WR016259.

Martinez, J.B., 1989. Simulación Matemática de Cuencas Subterráneas, Flujo Impermanente Bidimensional. CIH, ISPJAE, Ciudad La Habana.

Maxwell, R.M., Putti, M., Meyerhoff, S., Delfs, J.-O., Ferguson, I.M., Ivanov, V., Kim, J., Kolditz, O., Kollet, S.J., Kumar, M., Lopez, S., Niu, J., Paniconi, C., Park, Y.-J., Phanikumar, M.S., Shen, C., Sudicky, E.A., Sulis, M., 2014. Surface-subsurface model intercomparison: a first set of benchmark results to diagnose integrated hydrology and feedbacks. Water Resour. Res. 50, 1531–1549. https://doi.org/10.1002/2013WR013725.

Merz, B., Thieken, A.H., 2005. Separating natural and epistemic uncertainty in flood frequency analysis. J. Hydrol. 309, 114–132. https://doi.org/10.1016/j.jhydrol.2004.11.015.

Moench, A.F., Sauer, V.B., Jennings, M.E., 1974. Modification of routed streamflow by channel loss and base flow. Water Resour. Res. 10, 963–968. https://doi.org/10.1029/WR010i005p00963.

Moore, C., Doherty, J., 2005. Role of the calibration process in reducing model predictive error. Water Resour. Res. 41. https://doi.org/10.1029/2004WR003501.

Moriasi, D.N., Arnold, J.G., Van Liew, M.W., Binger, R.L., Harmel, R.D., Veith, T.L., 2007. Model evaluation guidelines for systematic quantification of accuracy in watershed simulations. Trans. ASABE 50, 885–900. https://doi.org/10.13031/2013.23153.

Mukolwe, M.M., Di Baldassarre, G., Werner, M., Solomatine, D.P., 2014. Flood modelling: parameterisation and inflow uncertainty. Proc. Inst. Civ. Eng. Manage. 167, 51–60. https://doi.org/10.1680/wama.12.00087.

Nash, J.E., Sutcliffe, J.V., 1970. River flow forecasting through conceptual models part I-A discussion of principles. J. Hydrol. 10, 282–290. https://doi.org/10.1016/0022-1694(70)90255-6.

Ogden, F.L., Lai, W., Steinke, R.C., 2014. ADHydro: Quasi-3D high performance hydrological model. Proc. SEDHYD 2015, 10th Interag. Sediment. Conf. 5th Fed. Interag. Hydrol. Model. Conf, Reno, Nevada, USA, pp. 19–23.

Ogden, F.L., Raj Pradhan, N., Downer, C.W., Zahner, J.A., 2011. Relative importance of impervious area, drainage density, width function, and subsurface storm drainage on flood runoff from an urbanized catchment. Water Resour. Res. 47, 1–12. https://doi.org/10.1029/2011WR010550.

Osei-Twumasi, A., Falconer, R.A., Ahmadian, R., 2016. Coupling surface water and groundwater flows in a laboratory model using foam as artificial groundwater material. Water Resour. Manage. 30, 1449–1463. https://doi.org/10.1007/s11269-016-1232-y.

Pahar, G., Dhar, A., 2014. A dry zone-wet zone based modeling of surface water and groundwater interaction for generalized ground profile. J. Hydrol. 519, 2215–2223. https://doi.org/10.1016/j.jhydrol.2014.09.088.

Panday, S., Huyakorn, P.S., 2004. A fully coupled physically-based spatially-distributed model for evaluating surface/subsurface flow. Adv. Water Resour. 27, 361–382. https://doi.org/10.1016/j.advwatres.2004.02.016.

Paniconi, C., Putti, M., 2015. Physically based modeling in catchment hydrology at 50: Survey and outlook. Water Resour. Res. 51, 7090–7129. https://doi.org/10.1002/2015WR017780.

Pappenberger, F., Beven, K., Horritt, M., Blazkova, S., 2005. Uncertainty in the calibration of effective roughness parameters in HEC-RAS using inundation and downstream level observations. J. Hydrol. 302, 46–69. https://doi.org/10.1016/j.jhydrol.2004.06.036.

Pappenberger, F., Matgen, P., Beven, K.J., Henry, J.-B., Pfister, L., Fraipont, P., 2006. Influence of uncertain boundary conditions and model structure on flood inundation predictions. Adv. Water Resour. 29, 1430–1449. https://doi.org/10.1016/j.advwatres.2005.11.012.

Pathiraja, S., Westra, S., Sharma, A., 2012. Why continuous simulation? the role of antecedent moisture in design flood estimation. Water Resour. Res. 48, 1–15. https://doi.org/10.1029/2011WR010997.

Pohlmann, F.K., 1987. An investigation of the Ground-Water Resources in the Wabash Valley Glacial Deposits near West Lafayette. Purdue University, Indiana.

Rawls, W.J., 2004. Pedotransfer functions for the United States. Dev. Soil Sci. 30, 437–447. https://doi.org/10.1016/S0166-2481(04)30023-1.

Rawls, W.J., Brakensiek, D.L., 1982. Estimating soil water retention from soil properties. J. Irrig. Drain. Div. 108, 166–171.

Rawls, W.J., Brakensiek, D.L., Saxtonn, K.E., 1982. Estimation of soil water properties. Trans. ASAE 25 1316–1320. https://doi.org/10.13031/2013.33720.

Saksena, S., 2015. Investigating the role of DEM resolution and accuracy on flood inundation mapping. In: World Environmental and Water Resources Congress 2015: Floods, Droughts, and Ecosystems. Proceedings of the 2015 World Environmental and Water Resources Congress, pp. 2236–2243. https://doi.org/10.1061/9780784479162.220.

Saksena, S., Merwade, V., 2017a. Integrated Modeling of Surface-Subsurface Processes to Understand River- Floodplain Hydrodynamics in the Upper Wabash River Basin. World Environ. Water Resour. Congr. 2017, ASCE, pp. 60–68. https://doi.org/10.1061/9780784480595.006.

Saksena, S., Merwade, V., 2017b. Deterministic approach to identify ordinary high water marks using hydrologic and hydraulic attributes. J. Irrig. Drain. Eng. 143, 1–15. https://doi.org/10.1061/(ASCE)IR.1943-4774.0001148.

Saksena, S., Merwade, V., 2015. Incorporating the effect of DEM resolution and accuracy for improved flood inundation mapping. J. Hydrol. 530, 180–194. https://doi.org/10.1016/j.jhydrol.2015.09.069.

Saleh, F., Flipo, N., Habets, F., Ducharne, A., Oudin, L., Viennot, P., Ledoux, E., 2011. Modeling the impact of in-stream water level fluctuations on stream-aquifer interactions at the regional scale. J. Hydrol. 400, 490–500. https://doi.org/10.1016/j.jhydrol.2011.02.001.

Schumann, G., Matgen, P., Hoffmann, L., Hostache, R., Pappenberger, F., Pfister, L., 2007. Deriving distributed roughness values from satellite radar data for flood inundation modelling. J. Hydrol. 344, 96–111. https://doi.org/10.1016/j.jhydrol.2007.06.024.

Schuol, J., Abbaspour, K.C., 2006. Calibration and uncertainty issues of a hydrological model (SWAT) applied to West Africa. Adv. Geosci. 9, 137–143. https://doi.org/10.5194/adgeo-9-137-2006.

Shokri, A., Bardsley, W.E., 2016. Development, testing and application of DrainFlow: A fully distributed integrated surface-subsurface flow model for drainage study. Adv. Water Resour. 92, 299–315. https://doi.org/10.1016/j.advwatres.2016.04.013.

Singhofen, P.J., Mcclung, G.L., 2014. Integrated 2D Surface-Groundwater Modeling of the Green Swamp. Proc. 2014 ESRI User Conf., FloridaSan Diego, CA.

Sorooshian, S., Duan, Q.Y., Gupta, V.K., 1993. Calibration of rainfall-runoff models - application of global optimization to the sacramento soil-moisture accounting model. Water Resour. Res. 29, 1185–1194. https://doi.org/10.1029/92WR02617.

Straatsma, M., Huthoff, F., 2011. Uncertainty in 2D hydrodynamic models from errors in roughness parameterization based on aerial images. Phys. Chem. Earth 36, 324–334. https://doi.org/10.1016/j.pce.2011.02.009.

Streamline Technologies, 2018. ICPR4 Technical Reference Manual. Streamline Technol. Inc., Winter SpringsFlorida www.streamnologies.com/misc/ICPR4_DOCS.zip.

Streamline Technologies, 2016. ICPR4 Validation Report. Streamline Technol. Inc., Winter Springs, Florida www.streamnologies.com/misc/ICPR4_DOCS.zip.

Teng, J., Jakeman, A.J., Vaze, J., Croke, B.F.W., Dutta, D., Kim, S., 2017. Flood inundation modelling: a review of methods, recent advances and uncertainty analysis. Environ. Model. Softw. 90, 201–216. https://doi.org/10.1016/j.envsoft.2017.01.006.

USGS, 2006. Estimated Percentage of Impervious Surface in Indiana in 2006, Derived from the 2006 National Land Cover Database (United States Geological Survey, 30-Meter TIFF Image). Indiana Geol. Surv.

VanderKwaak, J.E., Loague, K., 2001. Hydrologic-response simulations for the R-5 catchment with a comprehensive physics-based model. Water Resour. Res. 37, 999–1013. https://doi.org/10.1029/2000WR900272.

Vivoni, E.R., Ivanov, V.Y., Bras, R.L., Entekhabi, D., 2005. On the effects of triangulated terrain resolution on distributed hydrologic model response. Hydrol. Process. 19, 2101–2122. https://doi.org/10.1002/hyp.5671.

Weaver, C., Feaster, T., Robbins, J., 2016. Preliminary Peak Stage and Streamflow Data at Selected Streamgaging Stations in North Carolina and South Carolina for Flooding Following Hurricane Matthew, October 2016. United States Geol. Surv. 10.3133/ofr20161205 Open-File Rep. 2016-1205 38.

Wood, E.F., Sivapalan, M., Beven, K., Band, L., 1988. Effects of spatial variability and scale with implications to hydrologic modeling. J. Hydrol. 102, 29–47. https://doi.org/10.1016/0022-1694(88)90090-X.

Xie, Z., Su, F., Liang, X., Zeng, Q., Hao, Z., Yufu, G., 2003. Applications of a surface runoff model with horton and dunne runoff for VIC. Adv. Atmos. Sci. 20, 165–172.

Zehe, E., Blöschl, G., 2004. Predictability of hydrologic response at the plot and catchment scales: role of initial conditions. Water Resour. Res. 40, 1–21. https://doi.org/10.1029/2003WR002869.

Zhang, H.L., Wang, Y.J., Wang, Y.Q., Li, D.X., Wang, X.K., 2013. The effect of watershed scale on HEC-HMS calibrated parameters: a case study in the clear creek watershed in Iowa, US. Hydrol. Earth Syst. Sci. 17, 2735–2745. https://doi.org/10.5194/hess-17-2735-2013.